

Goddard Cumulus Ensemble Model. Part I: Model Description

WEI-KUO TAO¹ and JOANNE SIMPSON¹

(Manuscript received 21 September 1992, in final form 15 January 1993)

ABSTRACT

During the past two decades, convective scale models have advanced sufficiently to study the dynamic and microphysical processes associated with mesoscale convective systems. The basic features of these models are that they are non-hydrostatic and include a good representation of microphysical processes. The Goddard Cumulus Ensemble (GCE) model has been extensively applied to study cloud-environment interactions, cloud interaction and mergers, air-sea interaction, cloud draft structure and trace gas transport. The GCE model has improved significantly during the past decade. For example, ice-microphysical processes, and solar and infrared radiative transfer processes have been included. These model improvements allow the GCE model to study cloud-radiation interaction, cloud-radiation-climate relations and to develop rain retrieval algorithms for Tropical Rainfall Measuring Mission (TRMM). In Part I, a full description of the GCE model is presented, as well as several sensitivity tests associated with its assumptions. In Part II (Simpson and Tao, 1993), we will review GCE model applications to cloud precipitating processes and to the Tropical Rainfall Measuring Mission (TRMM), a joint U.S.-Japan satellite project to measure rain and latent heat release over the global tropics.

1. INTRODUCTION

During the past 20 years, observational data on atmospheric convection has been accumulated from measurements by various means, including radars, instrumented aircraft, satellites, and rawinsondes in special field observations (*e.g.*, GATE, PRE-STORM, COHMEX, TAMEX, EMEX and several others). This has made it possible for convective cloud modelers to test their simulations against observations, and thereby improve their models. In turn, the models have provided a necessary framework to relate the fragmentary observations to help in understanding the complex physical processes interacting in atmospheric convective systems, for which observations alone still cannot provide a dynamically consistent four-dimensional

¹ Mesoscale Dynamics and Precipitation Branch, Laboratory for Atmospheres,
NASA/Goddard Space Flight Center, Greenbelt, MD 20771, U.S.A.

picture. The past decades have also seen substantial advances in the numerical modeling of convective clouds and mesoscale convective systems (*e.g.*, squall-type and non-squall-type convective systems), which have substantially elucidated complex dynamical cloud-environment interactions in the presence of varying vertical wind shear. With the advent of powerful scientific computers such as the CRAY- YMP/C90, many important and complex processes (which require extensive computations), such as ice-microphysics and radiative transfer, can now be simulated to a useful (but still oversimplified) degree in these numerical cloud models.

A basic characteristic of the convective cloud models is that their governing equations are non-hydrostatic since the vertical and horizontal scales of convection are similar. Such models are also necessary in order to allow gravity waves, such as those triggered by clouds, to be resolved explicitly. Another requirement of these models is that they need increasingly sophisticated representation of microphysical processes, to which the dynamic processes have shown to be highly sensitive (Tao *et al.*, 1991; Ferrier *et al.*, 1992). The Goddard Cumulus Ensemble (GCE) model is one such model. Others have been developed by Klemp and Wilhelmson (1978), Cotton and Tripoli (1978), Schlesinger (1978), Clark (1979), Chen and Orville (1980), and Chen (1991).

The GCE model has been used to provide essential insights into the interactions of clouds with each other (Tao and Simpson, 1984; Tao and Simpson, 1989a), with their surroundings (Soong and Tao, 1980; 1984; Tao and Soong, 1986; Tao and Simpson, 1989b), with long wave radiative transfer processes (Tao *et al.*, 1991, 1993), with ocean surfaces (Tao *et al.*, 1991; Lau *et al.*, 1993; Sui *et al.*, 1993a and b), and with trace gas distributions (Scala *et al.*, 1990; Pickering *et al.*, 1991, 1992a, b, c). The GCE model has also been used to convert the radiances received by cloud-observing microwave radiometers into predicted rainfall rates (Simpson *et al.*, 1988). Remote sensing of cloud- top properties by high-flying aircraft bearing microwave and other TRMM instruments have already begun to provide a new and powerful means of testing the GCE model, particularly when such observations are augmented by simultaneous ground-based radar measurements (Adler *et al.*, 1988, 1991; Yeh *et al.*, 1992).

The Goddard Cumulus Ensemble Model's framework was originally based on the cloud ensemble model developed by Soong and Ogura (1980), Soong and Tao (1980), Tao (1983) and Tao and Soong (1986). However, many significant improvements have been made during the past decade at Goddard (it was named the GCE model in 1989). In this paper, we will present the full formulations (including the improvements) used in the GCE model, as well as several sensitivity tests associated with the assumptions. In Part II (Simpson and Tao, 1993), we will review GCE model applications to the study of cloud precipitating processes and to their measurement from space.

2. GODDARD CUMULUS ENSEMBLE MODEL

2.1 Equations of Motion

The derivation of the momentum equations requires the use of the moist equation of state, which is commonly written in the form

$$p = \rho RT(1 + 0.61q_v) \quad (1)$$

where p is the pressure, ρ the density of moist air, R the gas constant for dry air, T the temperature and q_v the mixing ratio of water vapor. The non-dimensional function of pressure is defined as

$$\pi = \left(\frac{p}{p_0}\right)^{R/C_p} \quad (2)$$

where P_0 is a reference pressure (1000 mb) and C_p the specific heat of dry air at constant pressure. The virtual potential temperature (θ_ν) is defined as

$$\theta_\nu = \theta(1 + 0.61q_\nu) \quad (3)$$

The potential temperature θ is related to π by $\theta = T/\pi$.

The x, y and z components of the momentum equations are written as

$$\frac{\partial u}{\partial t} = -\frac{\partial}{\partial x}uu - \frac{\partial}{\partial y}uv - \frac{1}{\bar{\rho}}\frac{\partial}{\partial z}\bar{\rho}uw - C_p\bar{\theta}\frac{\partial\pi'}{\partial x} + fv + D_u \quad (4)$$

$$\frac{\partial v}{\partial t} = -\frac{\partial}{\partial x}uv - \frac{\partial}{\partial y}vv - \frac{1}{\bar{\rho}}\frac{\partial}{\partial z}\bar{\rho}vw - C_p\bar{\theta}\frac{\partial\pi'}{\partial y} - fu + D_v \quad (5)$$

$$\frac{\partial w}{\partial t} = -\frac{\partial}{\partial x}uw - \frac{\partial}{\partial y}vw - \frac{1}{\bar{\rho}}\frac{\partial}{\partial z}\bar{\rho}ww - C_p\bar{\theta}\frac{\partial\pi'}{\partial z} + g\left(\frac{\theta'}{\bar{\theta}} + 0.61q'_\nu - q_l\right) + D_w \quad (6)$$

where u and v are the horizontal and w the vertical velocity components, g the acceleration of gravity and q_l the sum of the mixing ratios of liquid and ice water. A prime is defined as a deviation from the horizontal average. The subgrid-scale diffusion effects are represented by D_u , D_v and D_w which will be defined in Section 2.4.

The equations for θ and q_ν are written in the form

$$\begin{aligned} \frac{\partial\theta}{\partial t} = & -\frac{\partial}{\partial x}u\theta - \frac{\partial}{\partial y}v\theta - \frac{1}{\bar{\rho}}\frac{\partial}{\partial z}\bar{\rho}w\theta + D_\theta + \frac{L_v}{C_p}(c - e_c - e_r) + \frac{L_f}{C_p}(f - m) \\ & + \frac{L_s}{C_p}(d - s) + Q_R \end{aligned} \quad (7)$$

$$\frac{\partial q_\nu}{\partial t} = -\frac{\partial}{\partial x}uq_\nu - \frac{\partial}{\partial y}vq_\nu - \frac{1}{\bar{\rho}}\frac{\partial}{\partial z}\bar{\rho}wq_\nu + D_{q_\nu} + (c - e_c - e_r) + (d - s) \quad (8)$$

where L_v , L_f and L_s are the latent heats of condensation, fusion and sublimation, respectively. The variables c , e_c , e_r , f , m , d and s stand for the rates of condensation, evaporation of cloud droplets, evaporation of raindrops, freezing of raindrops, melting of snow and graupel/hail, deposition of ice particles and sublimation of ice particles, respectively. The term Q_R is the cooling/heating rate associated with radiative processes and will be discussed in Section 2.3. The subgrid-scale diffusion terms D_θ and D_{q_ν} will be defined in section 2.4.

2.2. Cloud Microphysical Processes

The cloud microphysics include a parameterized Kessler-type two-category liquid water scheme (cloud water and rain), and parameterized Lin *et al.* (1983) three-category ice-phase schemes (cloud ice, snow and hail/graupel). The shapes of liquid and ice are assumed to be spherical. Size distributions of rain (qr), snow (qs) and graupel (or hail) are taken to be inverse-exponential with respect to diameter (D) such that

$$N(D) = N_o \exp(-\lambda D) \quad (9)$$

where $N(D)$ is the number of drops of diameter between D and $D + \delta D$ in unit volume of space, N_o is the value of $N(D)$ for $D = 0$ (called intercept parameter), and $\lambda = (\frac{\pi \rho_x N_o}{\rho q_x})^{0.25}$ is the slope of the particle size distribution. The density and mixing ratio of the hydrometeors are ρ_x and q_x , respectively. The typical intercept parameters used in the GCE model for rain, snow and graupel (hail) are 0.08 cm^{-4} , 0.04 cm^{-4} , and 0.04 cm^{-4} (0.0004 cm^{-4}), respectively. The density for rain, snow and graupel (hail) are 1 g cm^{-3} , 0.1 g cm^{-3} , and 0.4 g cm^{-3} (0.917 g cm^{-3}), respectively. The cloud ice has a single size (mono-disperse) where its diameter and density are assumed to be $2 \times 10^{-3} \text{ cm}$ and 0.917 g cm^{-3} , respectively. The values of these parameters are based on limited observational data.

The predictive equations for cloud water (q_c), rain (q_r), cloud ice (q_i), snow (q_s) and graupel/hail (q_g) in the GCE model are:

$$\bar{\rho} \frac{\partial q_c}{\partial t} = -\frac{\partial}{\partial x} \bar{\rho} u q_c - \frac{\partial}{\partial y} \bar{\rho} v q_c - \frac{\partial}{\partial z} \bar{\rho} w q_c + \bar{\rho}(c - e_c) - T_{q_c} + D_{q_c} \quad (10)$$

$$\bar{\rho} \frac{\partial q_r}{\partial t} = -\frac{\partial}{\partial x} \bar{\rho} u q_r - \frac{\partial}{\partial y} \bar{\rho} v q_r - \frac{\partial}{\partial z} \bar{\rho}(w - V_r) q_r + \bar{\rho}(-e_r + m - f) - T_{q_r} + D_{q_r} \quad (11)$$

$$\bar{\rho} \frac{\partial q_i}{\partial t} = -\frac{\partial}{\partial x} \bar{\rho} u q_i - \frac{\partial}{\partial y} \bar{\rho} v q_i - \frac{\partial}{\partial z} \bar{\rho} w q_i + \bar{\rho}(d_i - s_i) - T_{q_i} + D_{q_i} \quad (12)$$

$$\bar{\rho} \frac{\partial q_s}{\partial t} = -\frac{\partial}{\partial x} \bar{\rho} u q_s - \frac{\partial}{\partial y} \bar{\rho} v q_s - \frac{\partial}{\partial z} \bar{\rho}(w - V_s) q_s + \bar{\rho}(d_s - s_s - m_s + f_s) - T_{q_s} + D_{q_s} \quad (13)$$

$$\bar{\rho} \frac{\partial q_g}{\partial t} = -\frac{\partial}{\partial x} \bar{\rho} u q_g - \frac{\partial}{\partial y} \bar{\rho} v q_g - \frac{\partial}{\partial z} \bar{\rho}(w - V_g) q_g + \bar{\rho}(d_g - s_g - m_g + f_g) - T_{q_g} + D_{q_g} \quad (14)$$

where V_r , V_s and V_g are the fall speeds of rain, snow and graupel, respectively, and $m = m_s + m_g$, and $f = f_s + f_g$. The cloud water and cloud ice will move with

the surrounding air. The terms T_{qc} , T_{qr} , T_{qi} , T_{qs} and T_{qg} are microphysical transfer rates between hydrometeor species, and their sum is zero. They are defined as:

$$T_{qc} = -(P_{sacw} + P_{raut} + P_{racw} + P_{sfw} + D_{gacw} + Q_{sacw} + Q_{gacw}) - P_{ihom} + P_{imlt} - P_{idw} \quad (15)$$

$$T_{qi} = -(P_{saut} + P_{saci} + P_{raci} + P_{sfi} + D_{gaci} + W_{gaci}) + P_{ihom} - P_{imlt} + P_{idw} \quad (16)$$

$$T_{qr} = Q_{sacw} + P_{raut} + P_{racw} + Q_{gacw} - (P_{iacr} + D_{gacr} + W_{gacr} + P_{sacr} + P_{gfr}) \quad (17)$$

$$T_{qs} = P_{saut} + P_{saci} + P_{sacw} + P_{sfw} + P_{sfi} + \delta_3 P_{raci} + \delta_3 P_{iacr} + \delta_2 P_{sacr} - [P_{gacs} + D_{gacs} + W_{gacs} + P_{gaut} + (1 - \delta_2) P_{racs}] \quad (18)$$

$$T_{qg} = (1 - \delta_3) P_{raci} + D_{gaci} + W_{gaci} + D_{gacw} + (1 - \delta_3) P_{iacr} + P_{gacs} + D_{gacs} + W_{gacs} + P_{gaut} + (1 - \delta_2) P_{racs} + D_{gacr} + W_{gacr} + (1 - \delta_2) P_{sacr} + P_{gfr} \quad (19)$$

where

$$W_{gacr} = P_{wet} - D_{gacw} - W_{gaci} - W_{gacs}$$

For $T > 273.16^\circ\text{K}$

$$P_{saut} = P_{saci} = P_{sacw} = P_{raci} = P_{iacr} = P_{sfi} = P_{sfw} = D_{gacs} = W_{gacs} = D_{gacw} = D_{gacr} = P_{gwet} = P_{racs} = P_{sacr} = P_{gfr} = P_{gaut} = P_{imlt} = 0 \quad (20)$$

For $T < 273.16^\circ\text{K}$

$$Q_{sacw} = Q_{gacw} = P_{gacs} = P_{idw} = P_{ihom} = 0 \quad (21)$$

δ_2 is defined as 1 for a grid box which has q_r and $q_s < 1 \times 10^{-4} \text{ g g}^{-1}$, and otherwise is defined as zero. δ_3 is defined as 1 for a grid box which has $q_r < 1 \times 10^{-4} \text{ g g}^{-1}$, and otherwise is defined as zero (see Lin *et al.*, 1983). D_{gaci} , D_{gacr} and D_{gacs} (W_{gaci} , W_{gacr} and W_{gacs}) are production rates for dry (wet) growth of hail. These microphysical processes are demonstrated in Figure 1 and explained in Table 1 (after Lin *et al.*, 1983; with slight modifications). The explicit formulation of these hydrometeor transformations can be found in Lin *et al.* (1983).

Table 1. Key to Figure 1.

<u>Symbol</u>	<u>Meaning</u>
Pdepi	Depositional growth of cloud ice.
Pint	Initiation of cloud ice.
Pimlt	Melting of cloud ice to form cloud water.
Pidw	Depositional growth of cloud ice at the expense of cloud water.
Pihom	Homogeneous freezing of cloud water to form cloud ice.
Piacr	Accretion of rain by cloud ice; producing snow or graupel depending on the amount of rain.
Praci	Accretion of cloud ice by rain; producing snow or graupel depending on the amount of rain.
Praut	Autoconversion of cloud water to form rain.
Pracw	Accretion of cloud water by rain.
Prevp (e_r)	Evaporation of rain.
Pracs	Accretion of snow by rain; producing graupel if rain or snow exceeds threshold and $T < 273.16$ or rain if $T > 273.16$.
P(Q)sacw	Accretion of cloud water by snow; producing snow (Psacw) if $T < 273.16$ or rain (Qsacw) if $T > 273.16$.
Psacr	Accretion of rain by snow; producing graupel if rain or snow exceeds threshold; if not, produces snow.
Psaci	Accretion of cloud ice by snow.
Psaut	Autoconversion (aggregation) of cloud ice to form snow.
Psfw	Bergeron process (deposition and riming) - transfer of cloud water to form snow.
Psfi	Bergeron process embryos (cloud ice) used to calculate transfer rate of cloud water to snow (Psfw).
Psdep (d_s)	Deposition growth of snow.
Pssub (S_s)	Sublimation of snow.
Psmilt (m_s)	Melting of snow to form rain, $T > 273.16$.
Pwacs	Accretion of snow by cloud water to form rain, $T > 273.16$.
Pgaut	Autoconversion (aggregation) of snow to form graupel.
Pgfr (f_g)	Probabilistic freezing (Bigg) of rain to form graupel.
D(Q)gacw	Accretion of cloud water by graupel.
D(W)gaci	Accretion of cloud ice by graupel.
D(W)gacr	Accretion of rain by graupel.
Pgsub (s_g)	Sublimation of graupel
Pgmlt (m_g)	Melting of graupel to form rain, $T > 273.16$. (In this regime, Qgacw is assumed to be shed as rain)
Pgwet	Wet growth of graupel; may involve Wgacs and Wgaci and must include Dgacw or Wgacr, or both. The amount of Wgacw which is not able to freeze is shed to rain.

into cloud water/cloud ice instantaneously when mixed-phase supersaturation occurs. The water/cloud ice is assumed to evaporate/sublimate instantaneously if the air is subsaturated. Precipitating rain drops (snow and graupel) evaporate (sublimate) only if the cloud water (cloud ice) is exhausted before saturation is attained. In application of this saturation adjustment, the terms, P_{ihom} , P_{idw} and P_{imit} , will be activated first. In addition, initiation of cloud ice (P_{int}) and depositional growth of cloud ice (P_{depi}) discussed in Rutledge and Hobbs (1984) will be used to initiate the cloud ice in a saturated environment. This procedure weighs the saturation mixing ratio in favor of ice at levels above the freezing level 0°C . This adjustment scheme will almost guarantee that the cloudy region (defined as the area which contains cloud water and/or cloud ice) is always saturated (100% relative humidity). This permits subsaturated downdrafts with rain and hail/graupel particles but not cloud-sized particles. Tao *et al.* (1989) presented the derivation (sensitivity) as well as the performance of the ice-water saturation adjustment scheme.

2.3 Radiative Transfer Processes

Short-wave (solar) and long wave (infrared) radiation parameterizations have recently been included in the GCE model. The long wave and short-wave radiative transfer calculations implemented in the GCE model were developed by Chou (1984, 1986) and Chou and Kouvaris (1991). This radiation scheme has also been applied in several General Circulation Models (*e.g.*, the UCLA-GLA GCM and the FSU global model). In computing the absorption of solar radiation by atmospheric gases, the spectrum is divided into two regions: short-wave ($< 0.69 \mu\text{m}$) and near infrared ($> 0.69 \mu\text{m}$). In the near infrared region, the computation of absorption of solar radiation by water vapor follows that of Chou and Arking (1981) and Chou (1986), which uses a broad band transmission parameterization for clear atmospheres and k-distribution approach for cloudy atmospheres. In the short-wave region, the computation of the absorption by ozone follows Lacis and Hansen (1974). The absorption by O_2 and CO_2 near the visible and near IR regions is included using the parameterization of Chou (1992). In cloudy atmospheres, the four-stream discrete ordinate of Stamnes *et al.* (1988) is used to compute transmittance and reflectance of cloudy layers. The adding method is then used to compute fluxes in a composite of clear and cloudy layers. The long-wave scheme takes into account the effects of both gaseous and hydrometeor absorption. For gaseous absorption, the effects of water vapor, carbon dioxide and ozone are computed.

It is necessary to parameterize the emissivity of gases and hydrometeors in order to simulate long-wave and short-wave radiative transfer processes. The parameterizations for water vapor and cloud effects are based on the commonly used broad-band emissivity method (see Stephens, 1978, 1984). Both liquid and solid phases of water as well as their size distributions are considered. In the water phase, the optical depth (τ) and effective emissivity ($\varepsilon_{eff}^{\uparrow\downarrow}$) of cloud are parameterized as

$$\tau = \frac{3 W_l}{2 r_e} \quad (22)$$

$$\begin{aligned} \varepsilon_{eff}^{\uparrow\downarrow} &= 1 - \exp(-a_o^{\uparrow\downarrow} W_l) \\ a_o^{\uparrow} &= 0.13; a_o^{\downarrow} = 0.158 \end{aligned} \quad (23)$$

where W_l is liquid water path (LWP; g m^{-2}) and r_e are the effective radius (micrometers) and are defined as follows:

$$r_e = \frac{\int_0^\infty n(r)r^3 dr}{\int_0^\infty n(r)r^2 dr} \quad (24)$$

$$W_l = \int_0^{\Delta\xi} W_l dz \quad (25)$$

where W_l is the liquid water content (g m^{-3}). For the ice-cloud, the optical depth and effective emissivity of cloud are parameterized following Starr and Cox (1985) and Ramaswamy and Ramanathan (1989), giving the relations:

$$\tau = 9.07 \times 10^{-2} W_i^{0.938} \quad (26)$$

and,

$$\begin{aligned} \varepsilon_{eff}^{\uparrow\downarrow} &= 1 - \exp(-b_o^{\uparrow\downarrow} W_i) \\ b_o^{\uparrow} &= 0.05; b_o^{\downarrow} = R_R b^{\downarrow} \end{aligned} \quad (27)$$

where W_i is ice water path (g m^{-2}); W_i is the ice water content (g m^{-3}); R_R is 1.6, 1.4 and 1.2 for the tropics, mid latitude day and mid latitude night, respectively. The effective radius of cloud water and cloud ice are specified to be 0.0003 and 0.002 cm, respectively. Model-predicted radiative cooling and heating rates at cloud top are on the order of 30 to 50°K/day, which is in good agreement with Stephens (1978). A quantitative estimate of the impact of radiative processes on the total surface precipitation as well as on the development and structure of squall lines will be presented in Part II.

2.4 Subgrid-scale Turbulence

The subgrid-scale turbulence used in the GCE model is based on work by Deardorff (1975), Klemp and Wilhelmson (1978), and Soong and Ogura (1980). In their approach, one prognostic equation is solved for subgrid kinetic energy (E), which is then used to specify the eddy coefficients (K_m). The effect of condensation on the generation of subgrid-scale kinetic energy is also incorporated in the model. The equation for the subgrid kinetic energy is written as

$$\frac{dE}{dt} = \overline{gw''} \left(\frac{\theta''}{\theta} + 0.61q_v'' - q_l'' \right) - \overline{u_i'' u_j''} \frac{\partial u_i}{\partial x_j} + \frac{\partial}{\partial x_j} \left(K_m \frac{\partial E}{\partial X_j} \right) - \frac{C_e}{l} E^{3/2} \quad (28)$$

where

$$\begin{aligned} E &= \frac{1}{2} \overline{(u_i'')^2} \\ \overline{u_i'' u_j''} &= \frac{2}{3} \delta_{ij} E - K_m \left(\frac{\partial u_i}{\partial x_j} + \frac{\partial u_j}{\partial x_i} \right) \\ K_m &= C_m E^{1/2} l \\ l &= (\Delta x \Delta y \Delta z)^{1/3} \end{aligned} \quad (29)$$

The terms on the right-hand side of equation (28) are stability, shear, diffusion and dissipation effects, respectively. The double overbar in the equation denotes an average over each grid point in the cloud model and double primed variables are the deviation from the grid values. The variables Δx , Δy and Δz are the grid intervals. The higher value of C_m and the lower value of C_e imply that stronger mixing will occur. The values $C_m=0.2$ and $C_e=0.7$ are used in the GCE model (Deardorff, 1975).

All the subgrid-scale terms have been defined except for the vertical buoyancy fluxes in a saturated area. These terms in a saturated area can be expressed as a function of the nearly conservative equivalent potential temperature θ_e and the total mixing ratio of water substance $q_t = q_v + q_c + q_i + q_r + q_s + q_g$. Following Klemp and Wilhelmson (1978), in a saturated area

$$\overline{w'' \left(\frac{\theta''}{\theta} + 0.61q_v'' - q_i'' \right)} = -AK_h \frac{\partial \theta_e}{\partial z} + K_h \frac{\partial q_t}{\partial z} \quad (30)$$

where

$$A = \frac{1}{\theta} \frac{1 + \frac{1.61\varepsilon L q_v}{R_d T}}{1 + \frac{\varepsilon L^2 q_v}{c_p R_d T^2}}$$

and $\varepsilon = 0.622$.

In an unsaturated area,

$$\overline{w'' \left(\frac{\theta''}{\theta} + 0.61q_v'' - q_i'' \right)} = -K_h \left(\frac{1}{\theta} \frac{\partial \theta}{\partial z} + 0.61 \frac{\partial q_v}{\partial z} \right) \quad (31)$$

Equation (31) is applied to both the cloud and subcloud layers wherever the air is not saturated. This term creates turbulent kinetic energy in the subcloud layer where the surface heat flux and evaporation maintain a slight instability. In the unsaturated portion of the cloud layer, this term produces a strong damping effect and destroys turbulent kinetic energy rapidly. The ratio $K_h/K_m=3$ was used in Klemp and Wilhelmson (1978). They also used the same K_h in both the horizontal and the vertical directions, implying an isotropic diffusion process. However, the ratio of K_h/K_m should actually decrease with increasing stability (Deardorff, 1973). Soong and Ogura (1980) incorporated the stability dependence of the ratio K_h/K_m and the anisotropy of turbulence by setting $K_h=2K_m$ everywhere except $K_h=3K_m$ in the vertical direction only at grid points where the sounding is unstable. Once the E , K_h and K_m are determined, the subgrid-scale terms can be computed from

$$\begin{aligned} D_{u_i} &= -\frac{\partial}{\partial x_j} \overline{u_i'' u_j''} \\ D_\theta &= -\frac{\partial}{\partial x_j} \overline{u_j'' \theta''} \approx \frac{\partial}{\partial x_j} \left(K_h \frac{\partial \theta}{\partial x_j} \right) \end{aligned} \quad (32)$$

The expressions for D_{q_v} , D_{q_c} , D_{q_r} , D_{q_i} , D_{q_s} , and D_{q_g} are similar to D_θ . Where a grid point is saturated, the following vertical turbulence diffusion equations are used:

$$\begin{aligned}
-\frac{\partial \overline{w''\theta''}}{\partial z} &\approx \frac{\partial}{\partial z} K_h \frac{\partial \theta_e}{\partial z} \times \left(1 + \frac{\varepsilon L^2 q_v}{c_p R_d T^2}\right)^{-1} \\
-\frac{\partial \overline{w''q_v''}}{\partial z} &\approx \frac{\partial}{\partial z} K_h \frac{\partial \theta_e}{\partial z} \times \left(1 + \frac{\varepsilon L^2 q_v}{c_p R_d T^2}\right)^{-1} \times \frac{\varepsilon L q_v}{R_d T \theta} \\
-\frac{\partial \overline{w''q_{c/i}''}}{\partial z} &\approx \frac{\partial}{\partial z} w'' q'' + \frac{\partial}{\partial z} K_h \frac{\partial q_t}{\partial z}
\end{aligned} \tag{33}$$

The derivation of these equations can be found in Klemp and Wilhelmson (1978).

2.5 Heat and Moisture Fluxes from the Ocean surface

Surface heat and moisture are included in the diffusion terms D_θ and D_{q_v} at the lower boundary of the model obtained from bulk formulations. The vertical flux of sensible heat from the sea surface is assumed to take the form

$$\overline{(w''\theta'')}_{\circ} = -C_D V_o (T_s - T_o) / \bar{\pi} \tag{34}$$

where C_D is the drag coefficient, V_o the surface wind speed, T_s the sea surface temperature, and T_o the air temperature at the anemometer level. The GCE model uses the formulation by Roll (1965) for the drag coefficient, namely:

$$C_D = (1.10 + 0.04V_o) \times 10^{-3} \tag{35}$$

where V_o is in meters per second. The moisture flux from the sea surface has a similar form

$$\overline{(w''q_v'')}_{\circ} = -C_D V_o (q_s - q_o) \tag{36}$$

where q_o is the mixing ratio at the anemometer level and q_s is the saturation mixing ratio at the sea surface temperature. In the model computations, the values of V_o , T_o and q_o are taken from the lowest grid level.

2.6 Model Domain, Numerical Technique, and Boundary Conditions

A stretched vertical coordinate (height increments from 220 to 1050 m) with 31 grid points is used in order to maximize resolution in the lowest levels. The model top can be 20-25 km. For a typical two-dimensional simulation, 612 grid points were used in the horizontal, the central 504 of which comprise the fine-grid area with a constant 750 m resolution. Simulated cloud activity is confined to the fine-grid region through a Galilean transformation, namely by subtracting the storm propagation speed from the initial wind field. Outside of this region, the grid is horizontally stretched with a ratio of 1.0625:1 between adjacent grid points. This results in a domain that is about 1025 km wide. A staggered-grid arrangement (Arakawa C grid) is used in the model. A leapfrog time integration and second-order space derivative scheme in the vertical direction are used. Either a second- or a fourth-order space derivative scheme (Chen, 1980) is used in the horizontal direction. To avoid the problem of time-splitting, a time smoother is adopted. The time smoothing coefficient is set to 0.1 with a time interval of 7.5 s.

Open-type lateral boundary conditions are most frequently used (Klemp and Wilhelmson, 1978). The goal was to allow the advection of the normal velocity component out

through the boundary at a speed given by the sum of the normal velocity component and an approximated intrinsic phase velocity c^* of the dominant gravity wave modes with minimum reflection. An approximation for the normal velocity equation at an outflow boundary location is given by

$$\frac{\partial u}{\partial t} + (u + c^*) \frac{\partial u}{\partial x} = 0 \quad (37)$$

where c^* must be selected in some way. Klemp and Wilhelmson (1978) suggested the c^* might be about 30 m s^{-1} . Chen (1982), however, found that in some cases a c^* less than 30 m s^{-1} leads to a better comparison (small domain versus larger ones), particularly in some three-dimensional tests. The use of stretched horizontal coordinates causes the model results to be less sensitive to the choice of gravity wave speed associated with the open lateral boundary conditions (Fovell and Ogura, 1988). A free-slip boundary condition is used for u , v , θ , q_v , and all five water hydrometeors. The w -velocity is set to zero. A 5 km deep Rayleigh relaxation (absorbing) layer is also used at the top of the model.

In the three-dimensional model, however, the current computer limits us to about 218×54 grid points (using 1 or 1.5 km resolution) in the horizontal and 32 grid points (to a depth of 22 km) in the vertical. For line-type convection, an open-type lateral boundary condition is used along the x -axis in the direction perpendicular to the line convection and a periodic lateral boundary condition is applied along the y -axis. However, open lateral boundary conditions can also be used on the y -axis for simulating isolated storms (*e.g.*, super-cells). In actual computation, the number of grid points in each simulation can be adjusted for specific purposes and economy of computer time.

3. SENSITIVITY TESTS

3.1 Microphysical Processes

3.1.1 Ice versus no-ice runs

To investigate the role of ice-phase microphysics in stratiform precipitation, a no-ice-phase version of the GCE model, with a Kessler-type two-category liquid water microphysics, was utilized for a GATE squall line simulation (Tao and Simpson, 1989b). The system's life cycle and total precipitation do not differ significantly from the ice run (see Table 2). The modeled propagation speed of about 8.2 m s^{-1} differs only slightly from that of the ice run. These results suggest that the ice-phase microphysical processes do not significantly affect the propagation speed of the simulated systems. From a close examination of the model results, it was found that the propagation speed of the modeled systems is closely related to the proximity and vigor of simulated downdrafts and their associated cold outflow structure in the lower troposphere. The total amount of evaporative cooling in the stratiform and convective regions in the ice-free-run does not change significantly from the run with ice in these particular GATE simulations. The small difference (< 1 to 2 m s^{-1}) in simulated squall line propagation speeds for the runs with and without ice-phase processes were also reported in Yoshizaki (1986), Nicholls (1987), Fovell and Ogura (1988) and Chen (1991). In each study, the surface wind gust, temperature drop, and pressure rise, which are all usually associated with cold outflow, are quite similar between the runs with and without ice-phase processes.

Table 2. Estimated surface rainfall and rainfall area at the surface. Rain is given in relative units (millimeters per grid point accumulated over a 12 h period). The total rain area is given as a percentage of the total domain area. Anvil portion and anvil rain area are given as a percentage of the total rain and total rain area, respectively.

(GATE Squall Line Simulations)

	Total-Rain (mm/grid/12h)	Stratiform Portion	Total Rain Area (%)	Stratiform Rain Area(%)
Ice-run	24.91	32.7%	22.3	86.8
Ice-free	23.42	11.5%	8.1	66.1

Several differences, however, are noted between the ice run and the ice-free run. The first difference concerns the precipitation statistics of simulated squall MCSs. It was found that light rain ($< 10 \text{ mm h}^{-1}$) only accounts for about 26.5% of the total rain, but it covers 90% of the total rain area for the ice run. By contrast, heavy precipitation ($> 30 \text{ mm h}^{-1}$) accounts for a large portion of the total rain, but it only occupies a very small portion of the total rain area. Without the inclusion of ice-phase microphysics, the role of heavy precipitation is increased significantly. Also, only 12% of the rain is characterized as stratiform (Figure 2). The model results with ice-phase microphysics are generally in good agreement with GATE observations (see Table 1 in Tao and Simpson, 1989b). Another difference is that the depth of the stratiform cloud is reduced with ice-free microphysics. More cellular rather than mesoscale features are also evident for the ice-free run (Figure 3). In a separate modeling study of a subtropical squall line that occurred during TAMEX (Tao *et al.*, 1991), it was found that a slower propagation speed resulted from the run without ice processes. However, the simulated squall system did not last long (decayed about 5 h into the simulation). The rain fell into the front inflow region and cut off the moisture supply in the ice-free run. The updraft tilted downshear in relation to the low-level shear. As reported in many modeling and observational studies, an upshear tilt of the updraft is a necessary condition for a long lasting convective system.

3.1.2 Ice scheme comparisons

The GCE model has been used to investigate different ice-phase microphysical parameterization schemes as well as their effects on convective motion under different tropical environmental conditions (McCumber *et al.*, 1991). Two specific experiments from McCumber *et al.* will be presented here. The first one adapted the Lin *et al.* (1983) scheme which includes hail processes. Intercept parameter for snow (Nos), hail (Noh) and density of hail (ρ_g) are 0.03 cm^{-4} , 0.0004 cm^{-4} and 0.917 g cm^{-3} , respectively. These parameters were typical for mid latitude convective clouds. In the second experiment, Nos, Noh and ρ_g are 0.04 cm^{-4} , 0.04 cm^{-4} and 0.4 g cm^{-3} , respectively, which were used for warm frontal cloud simulations (Rutledge and Hobbs, 1984). The graupel has a low density and a large intercept (i.e., high number concentration). By contrast, the hail has a high density and a small intercept (low number concentration). These differences affect not only the description

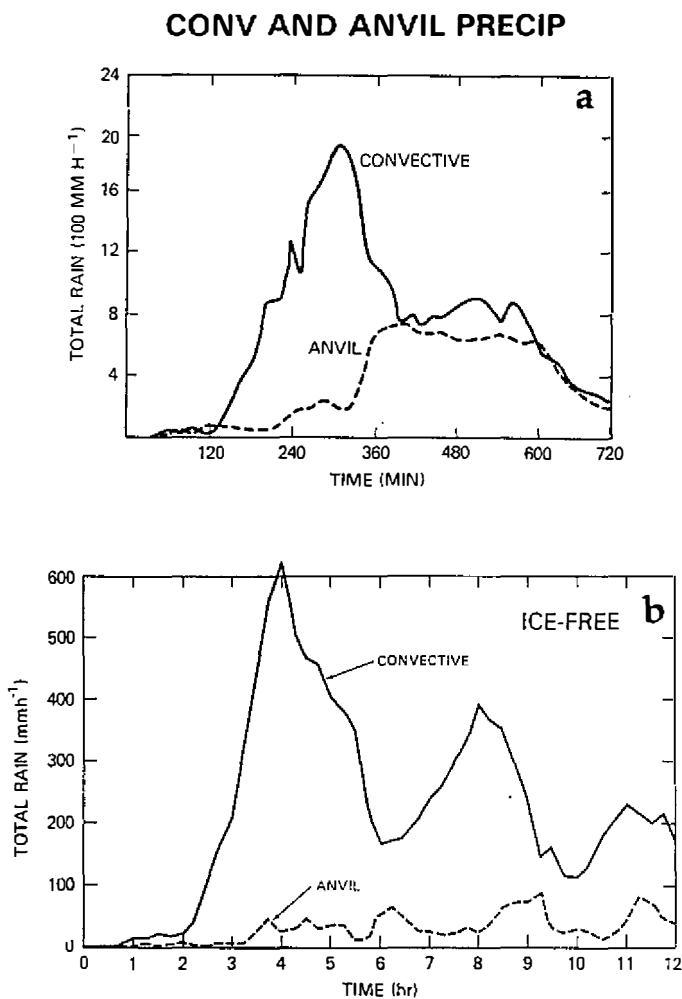


Fig. 2. Total rain intensity integrated over the grid points designated as the convective and stratiform (anvil) regions. (a) Ice run, and (b) ice-free run.

of the hydrometeor population, but also the relative importance of the microphysical processes (Figure 4). For example, in the hail case, the value selected results in a few large, fast-falling hail stones. These characteristics confine hail to the convective cells. A result of this is that snow becomes the dominant precipitating hydrometeor type in the anvil cloud. The large amount of snow (Figures 4a and 5b) is the reason why melting and deposition of snow are first-order processes for the hail case. In the graupel case, however, the selected parameter values result in a large number of graupel particles that are smaller than the hail particles and thus fall more slowly. These characteristics permit graupel to occur in both the convective cell and the anvil. Also note that in the anvil graupel is much more prevalent than snow (Figure 5a). For this reason, melting and deposition of snow are second-order processes. For the tropical squall-type convective systems, the principal distinction in the heating profiles

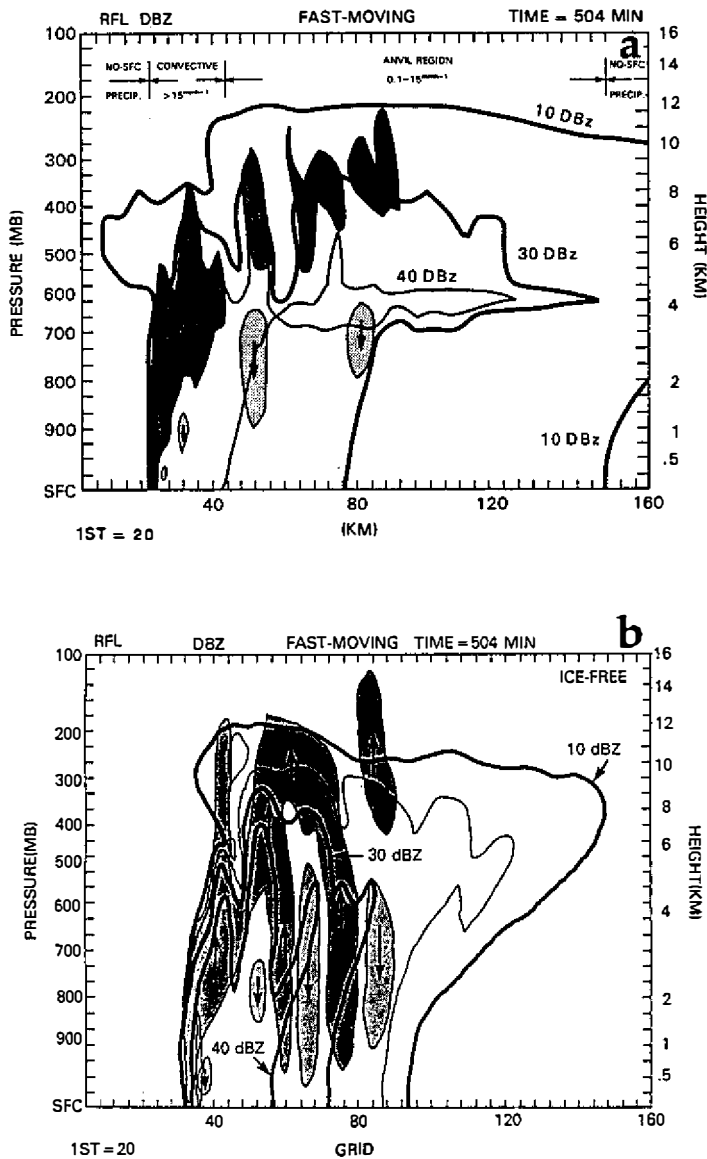


Fig. 3. Vertical cross section of a simulated tropical squall-type convective line at its mature stage. The heavy solid lines indicate the 10, 30 and 40 dBZ radar reflectivity contours. In the dark shaded area, $w > 0.5 \text{ m s}^{-1}$, and in the light shaded area, $w < -0.5 \text{ m s}^{-1}$. The convective, stratiform and no-surface precipitation regions are also indicated. (a) Ice run, and (b) ice-free run.

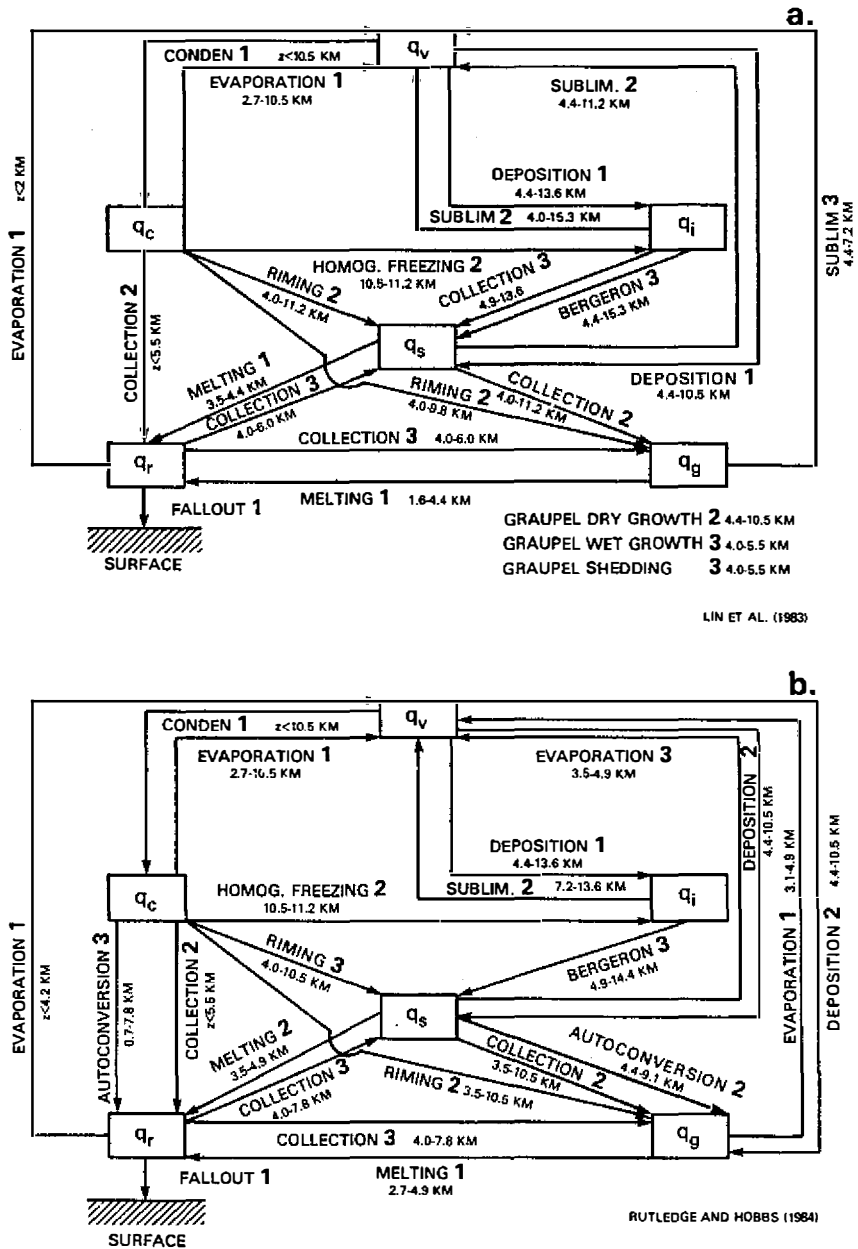


Fig. 4. Process diagrams for the microphysics used in three-class ice schemes. Only those microphysical processes are shown that are of the highest three orders of importance (order is indicated by the large numerals). Order is determined from summing the contributions of each process over all grid points at each vertical level and over the entire 12-h simulation time. Also shown is the layer in the vertical, applicable to each process for the order of importance given. (a) Hail case, and (b) graupel case.

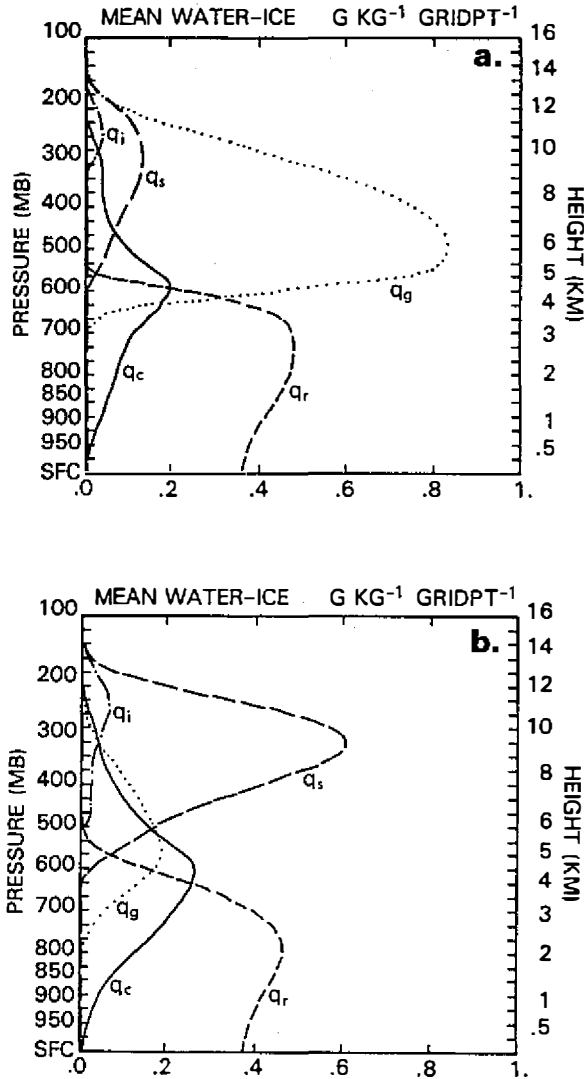


Fig. 5. Mean water and ice hydrometeors (g kg^{-1} per grid point) depicted as a function of height for tropical squall system simulations. The curves for the hydrometeors shown are rain q_r (short dash), cloud water q_c (solid), graupel/hail q_g (dotted), cloud ice q_i (dot-dash), and snow q_s (long dash). The units in the figure are normalized with respect to the number of horizontal model grid points. (The unnormalized units are obtained by multiplying by 512 km). (a) Graupel case, and (b) hail case.

between the hail and graupel case is the shape and intensity of the heating/cooling component in the anvil region (Figure 6). The cooling in the anvil region from the freezing level at about 4.5 km down to about 2 km in Figure 6a indicates the significance of melting graupel particles. Significantly less cooling due to melting in the anvil region for the hail case (Figure 6b) as opposed to the graupel case suggests that for the tropical squall system, the optimal mix of three-class ice hydrometeors is cloud ice-snow-graupel. A similar conclusion was reached for a TAMEX squall line simulation (Tao *et al.*, 1991). Recently, Sui *et al.* (1993a) have found a distinct minimum in the temperature lapse rate near 4.5 km level in the GATE and Western Pacific regions. They suggested that this minimum could be caused by melting processes.

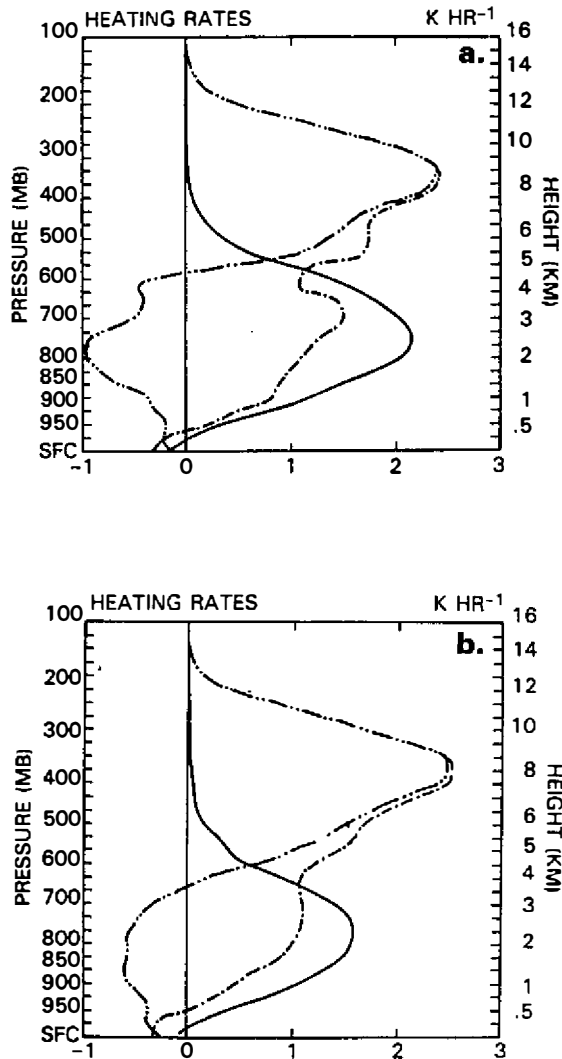


Fig. 6. Convective heating profiles (K h^{-1}) computed for the last 5 h of 2D simulations for tropical squall-type convective lines. Shown are the heating in the convective region (solid), heating in the anvil region (double dot-dash), and the total heating (dot-dash). (a) Graupel case, and (b) hail case.

Another characteristic that is sensitive to the parameterization of cloud microphysics is the passive microwave signatures that result from the cloud hydrometeors (*e.g.*, Figure 5). Simpson *et al.* (1988) and Adler *et al.* (1991) showed that vertical profiles of water and ice particles predicted by the cloud model can be used in a passive radiative transfer model to calculate the black body temperatures corresponding to signals detected by remote aircraft or satellite-borne sensors, and could be done simultaneously for several important microwave frequencies. Their response is particularly sensitive to the concentration and properties of large ice (Smith and Mugnai, 1989). Since the GCE model is used in rain and latent heat retrieval algorithms based on passive microwave (Adler *et al.*, 1989), it is very important to properly represent the vertical profile of hydrometeors. To appreciate this point, consider again the vertical hydrometeor profiles in Figure 5. The variability that they display as a function of different microphysical formulations provides some hint of the impact of different ice schemes on passive microwave characteristics, which is discussed in more detail in Part II.

3.2 Anelastic and Compressible Systems

The Goddard Cumulus Ensemble (GCE) modeled flow can be either anelastic (Ogura and Phillips, 1962), filtering out sound waves, or compressible (Klemp and Wilhelmson, 1978), which allows the presence of sound waves. The sound waves are not important in thermal convection, their processes can place severe restrictions on the time step in numerical integrations because of their high propagation speed. For this reason, most cloud modelers use an anelastic system of equations in which sound waves have been removed by eliminating certain terms in the compressible system (*e.g.*, neglecting the local variation of air density with time in the mass continuity equation).

In the anelastic approximation the continuity equation is:

$$\frac{\partial u}{\partial x} + \frac{\partial v}{\partial y} + \frac{1}{\bar{\rho}} \frac{\partial \bar{\rho} w}{\partial z} = 0 \quad (38)$$

A diagnostic pressure equation can be determined for the anelastic set by differentiating (4) with respect to x , (5) with respect to y and (6) with respect to z . Because the boundary conditions for the pressure equation are of the Neumann type (*i.e.*, they involve pressure derivatives), there are an infinite number solutions to the elliptic pressure equation that differ from one another by some constant. This is not a problem because only the derivatives of pressure are needed in the model equations (4-6). The elliptic pressure equation can be solved using direct (*e.g.*, FFT) or iterative methods. However, when terrain is added, the direct methods become more complex and sometimes time consuming.

In the compressible system, the pressure equation is derived by taking the substantial derivative of (2) and using the compressible continuity equation

$$\frac{\partial \rho}{\partial t} + \frac{\partial}{\partial x_j} \rho u_j = 0 \quad (39)$$

to eliminate $\frac{d\rho}{dt}$ and the thermodynamic equation (7) to remove $\frac{d\theta}{dt}$. The resulting equation is

$$\frac{\partial \pi'}{\partial t} + \frac{\bar{c}^2}{c_p \bar{\rho} \bar{\theta}_v^2} \frac{\partial}{\partial x_j} \bar{\rho} \bar{\theta}_v u_j \approx 0 \quad (40)$$

where c is the speed of sound given by $\bar{c}^2 = c_p R_d \bar{\pi} \bar{\theta}_v / c_v$. Due to the presence of sound waves, a very small time step, 2 s, for a 1000 m spatial resolution is needed for time integration of the entire model equation set. However, Klemp and Wilhelmson (1978) developed a semi-implicit time-splitting scheme, in which the equations are split into sound-wave and gravity-wave components, to achieve computational efficiency. The small time step integration is semi-implicit in the vertical using a 2 s time step. The remaining time integration can use a 10 s time-step. One advantage of the compressible system is its computational simplicity and flexibility. The numerical code then remains a set of explicit prognostic equations and alterations involving such things as stretched or nested grids, surface terrain and boundary conditions (*e.g.*, radiative upper boundary) can be incorporated into the numerical model without complicating the solution procedure (Klemp and Wilhelmson, 1978).

Anderson *et al.* (1985) have tested an anelastic system using a 4 s time step against the results from a fully compressible system without using the time-splitting technique (which needs a 0.3 s time step). They have found that the anelastic system produced essentially identical results to those of the compressible system for 2-D cool pool experiments lasting 500 s, where the convection was initiated by a cool pool. Ikawa (1988) has also compared the anelastic and the compressible system with a 2-D case involving orography. His results indicated that both simulated systems are similar if sound waves are damped enough in the compressible system. Due to the stretched grid arrangement in the horizontal (Section 2.6), the three-dimensional version of the GCE model (which has open lateral boundary conditions and a stretched grid) adapted the compressible system. All of the two-dimensional GCE simulations (including published results) used the anelastic system. A pair of sensitivity tests, anelastic versus compressible, were performed with an initial condition associated with a PRE-STORM squall line (Figure 1 in Tao *et al.*, 1993). All model physics are activated in these two runs for a 12 h time simulation in order to maximize the possibility of differences. Figure 7 shows that the GCE model does not produce identical results. The differences between the anelastic and compressible systems are much smaller, however, than those obtained by changing microphysical processes and advection schemes (Section 4.2). The precipitation statistics (*e.g.*, total precipitation and its stratiform component) from the anelastic and the compressible systems are also quite similar especially during the first 4 h (Table 3). Several observed features for this PRE-STORM squall system, such as the propagation speed of the squall system, the weakly evolving multicellular structure, the mesolow aloft, the squall pressure high, and the rear inflow from the midtroposphere, were well-simulated in both systems. No significant differences were found in simulated cloud updraft/downdraft structure and cloud top height between the two systems. It is difficult to tell which method is the most promising or will prevail in the future.

Table 3. Surface rainfall accumulated over 4 h, 8 h and 12 h simulations for the anelastic and compressible systems, and normalized with respect to the total model domain (P_o in mm/grid/4 h). Anvil portion is given as percentage of the total rain.

(PRE-STORM Squall Line Simulations)				
Time	Anelastic		Compressible	
	Rain	Anvil	Rain	Anvil
0-4h	2.48	5.6%	2.50	6.1%
4-8h	4.45	17.1%	4.57	14.8%
8-12h	4.62	22.4%	4.57	23.8%
0-12h	11.54	16.8%	11.64	16.5%

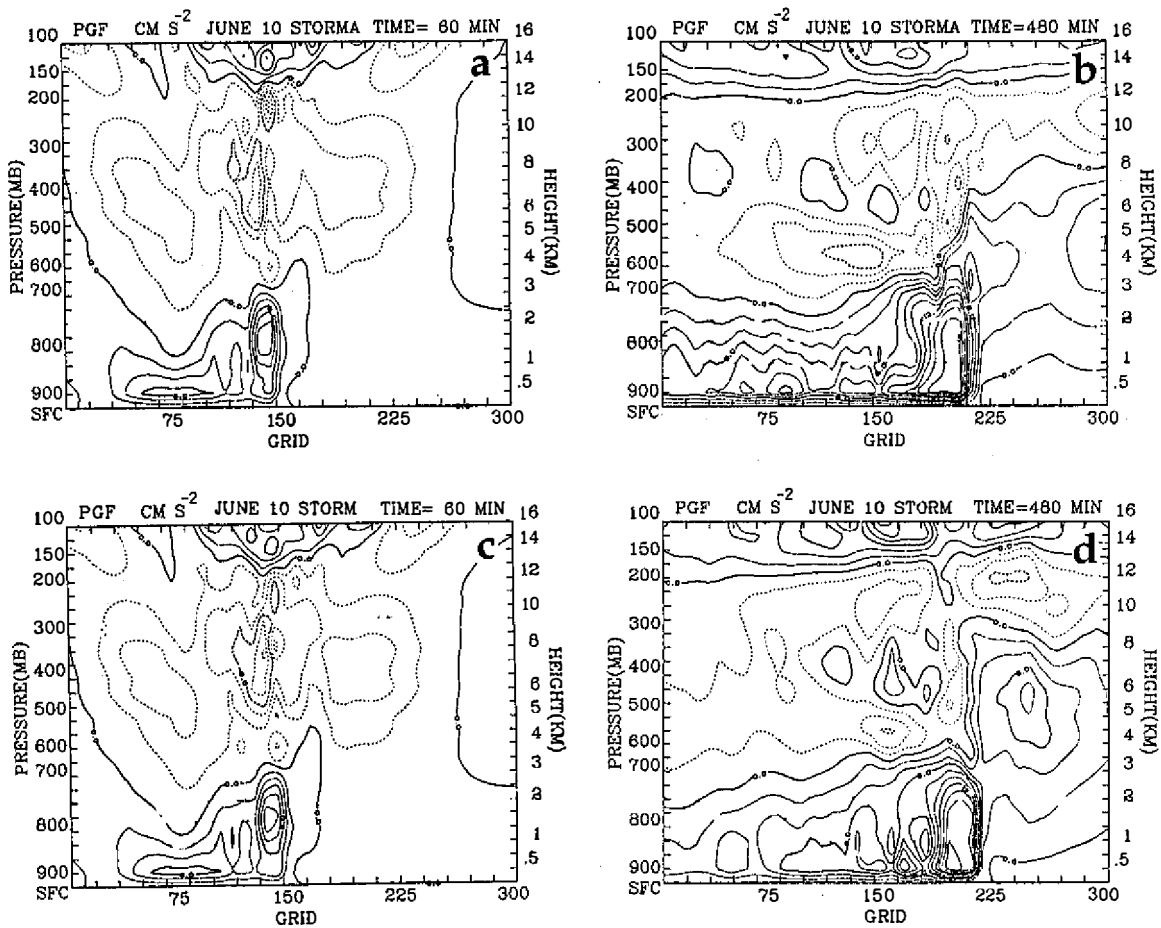


Fig. 7. Vertical cross section of the pressure gradient force term in the w -momentum equation over part of the model domain at (a) 60 min and (b) 480 min for a simulated mid latitude squall-type convective line using the anelastic assumption. (c) and (d) are the same as (a) and (b), respectively, except for the compressible system.

3.3 Two-(2-D) versus Three-Dimensional (3-D) Simulations

Ideally, three-dimensional model simulations are necessary for studying the relationship between vertically varying environmental winds and such features as rotation within and orientation of updrafts and downdrafts, cloud movement relative to the mean wind direction, and flow of the environmental wind around a cloud. However, doubling the number of grid points in a three-dimensional domain implies an eight fold increase in computer time, which exceeds the computing power currently available. Mesoscale convective systems (*e.g.*, squall lines) can cover a very large area (300–400 km in width and 1000 km in length). Both two- and three-dimensional simulations thus need to be run in combination.

Tao *et al.* (1987) used 2-D and 3-D versions of the GCE model to study the statistical properties of cloud ensembles for a well-organized intertropical convergence zone (ITCZ) rainband that occurred during GATE. The statistical properties of clouds, such as mass flux by cloud drafts and vertical velocity as well as condensation and evaporation have been examined. Figure 8 shows heating rates by condensation (c) and evaporation (e) in the 2-D model and the 3-D model. The heating rate estimated from large-scale observations, $Q_1 - Q_R$, and the total cloud heating rate in the 3-D model are also included. The rate of condensation in the 3-D case is slightly larger than its 2-D counterpart, but so is the rate of evaporation. As consequence, the net heating effect of clouds in the 3-D model is nearly equal to the 2-D counterpart, and both of them agree with $Q_1 - Q_R$ as estimated from the large-scale heat budget. (Note a minimum in the observed heating profile near 700 mb as discussed in Section 3.1).

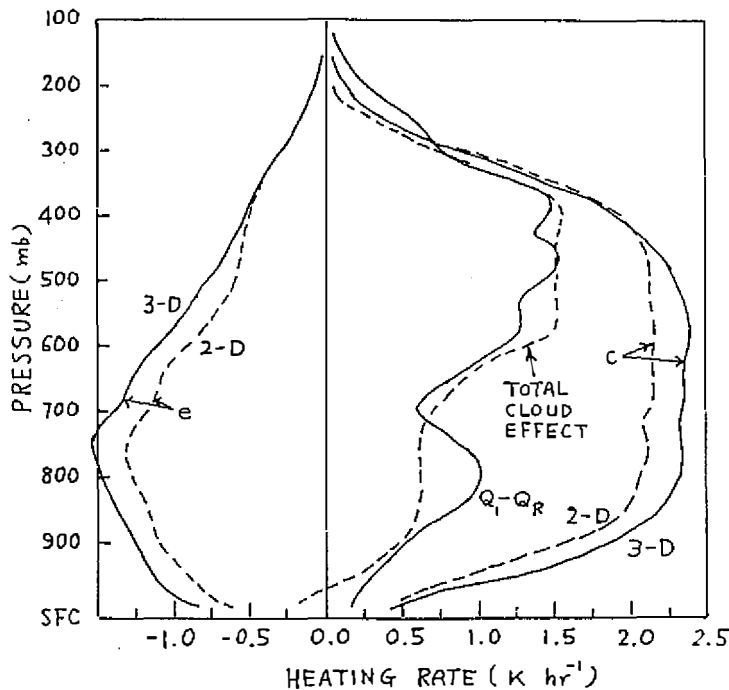


Fig. 8. Heating rates for condensation, c, and evaporation, e, in the two-dimensional model (dashed line) and the three-dimensional model (solid line). The heating rate estimated from the large-scale observations, $Q_1 - Q_R$, and the total cloud heating rate in the three-dimensional model are also included.

Zipser and LeMone (1980) and LeMone and Zipser (1980) presented the results of statistical analyses of convective updrafts and downdrafts. Their analysis is based on aircraft data gathered from cumulonimbus cloud penetrations for six days during GATE. In order to facilitate a comparison between our model results and their analysis, we have subdivided

the updrafts and downdrafts into active or inactive updrafts and downdrafts (Table 4). For example, a grid point in the model is designated as an active updraft region if (a) the total liquid water content exceeds 0.01 g kg^{-1} and (b) the vertical velocity is larger than 1 m s^{-1} (or 2 m s^{-1} , depending upon how we define "active") at that grid point and at that integration time. The inactive and active cloud fractional area coverage's as determined by aircraft measurement and model results are shown in Table 5. These ratios between active cloud updrafts and downdrafts indicate an excellent agreement among results between 2-D and 3-D models as well as the cores as measured by Zipser and LeMone (1980). Both 2-D and 3-D model results also showed a similar feature in that the active updrafts account for approximately 75% of the upward mass flux due to clouds and yet they only cover about 12-14% of the total area. This result is consistent with the concept, first proposed by Riehl and Malkus (1958; see also Riehl and Simpson, 1979), that hot towers play a critical role in the heat and moisture budgets in the tropics, even though they occupy a small fraction of the area. Overall, our comparison study has indicated that the statistical properties of the clouds obtained in the 2-D model are essentially the same as the 3-D counterpart given an identical large-scale environment (see Tao, 1983).

In another GATE squall line simulation, Tao and Simpson (1989b) found that the three-dimensional model results could not adequately reproduce many of the features associated with the stratiform region due to a small domain as well as a shorter time integration (4h). The orientation of the three-dimensional simulated convective line is perpendicular to the environmental wind shear as observed during GATE. Both 2-D and 3-D modeled propagation speeds are in fair agreement with observational studies. Based on the trajectory analyses, it was also found that the air circulation near the leading edge of a squall-type system is very similar in both the two and three-dimensional model simulations. This conclusion is consistent with the results of Rotunno *et al.* (1988) and Moncrieff (1992). However, all of these conclusions were based on simulations of well-organized convective lines.

Table 4. Calibration of clear, active and inactive cloud drafts. b is either 1 or 2 m s^{-1} .

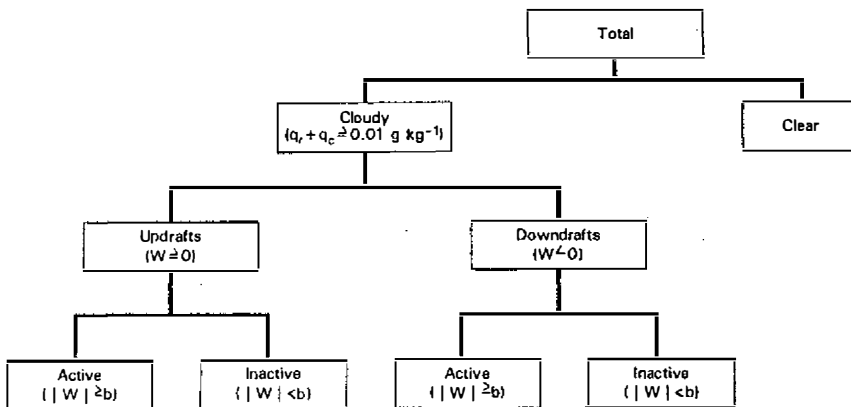


Table 5. Ratio of fractional cloud coverage ($R = \text{cloud updraft coverage} / \text{cloud downdraft coverage}$). Fractional coverage occupied by cloud drafts and active cloud drafts over the domain are also shown within the parentheses.

Altitude Range (m)	Zipser and LeMone		Two-D			Three-D		
	Draft	Core	Cloudy	Active 1ms ⁻¹	Active 2ms ⁻¹	Cloudy	Active 1ms ⁻¹	Active 2ms ⁻¹
9500			1.36 (34.6/25.4)	2.92 (2.98/1.02)	8.00 (1.60/0.20)	1.60 (45.9/28.8)	1.98 (2.87/1.35)	8.60 (1.54/0.18)
4300-8100	0.57 (16.9/29.9)	2.56 (4.6/1.8)	1.04 (11.3/10.9)	2.80 (4.2/1.5)	12.70 (2.8/0.22)	0.81 (11.7/14.4)	2.87 (4.3/1.5)	22.20 (2.89/0.13)
2500-4300	0.60 (18.3/30.3)	1.30 (2.1/1.1)	0.75 (8.4/11.2)	1.05 (4.1/3.9)	2.45 (2.7/1.1)	0.58 (8.3/14.3)	1.23 (3.8/3.1)	7.21 (2.81/0.39)
700-2500	0.65 (16.3/25.2)	1.91 (2.1/1.1)	1.07 (13.9/12.9)	1.37 (4.1/3.0)	2.63 (2.1/0.8)	0.76 (13.4/17.0)	1.72 (4.3/2.5)	4.90 (2.45/0.50)
300-700	0.88 (16.6/18.8)	1.88 (1.5/0.8)	1.13 (15.3/13.5)	1.24 (2.47/2.00)	2.03 (0.73/0.36)	0.95 (17.2/18.2)	1.68 (3.2/1.9)	3.40 (0.85/0.25)
0-300	1.01 (15.9/15.7)	1.50 (0.3/0.2)	1.11 (15.6/14.0)	1.36 (0.87/0.64)	1.78 (0.16/0.09)	0.99 (17.6/17.8)	1.38 (1.1/0.8)	1.20 (0.12/0.10)

$$R = \frac{U}{D}$$

U = Updraft area coverage in %

D = Downdraft area coverage in %

R = U/D (Ratio between updraft area coverage and downdraft area coverage)

4. MODEL IMPROVEMENTS

4.1 Double-moment Multi-phase Four-class Ice Scheme (4ICE)

A new microphysical parameterization has been developed recently by Ferrier (1993) and Ferrier *et al.* (1993), which combines the main features of previous three-class ice schemes by calculating the mixing ratios of both graupel and frozen drops/hail. Additional model variables include the number concentrations of all ice particles (small ice crystals, snow, graupel and frozen drops), as well as the mixing ratios of liquid water in each of the precipitation ice species during wet growth and melting for purposes of accurate active and passive radiometric calculations. The parameterization also includes the following: (1) more accurate calculation of accretion processes, including partitioning the freezing of raindrops as sources of snow, graupel and frozen drops/hail; (2) consideration of rime densities and riming rates in converting between ice species due to rapid cloud water riming; (3) incorporation of new parameterizations of ice nucleation processes, the rime splintering mechanism using laboratory data, and the aircraft observations of high ice particle concentrations; (4) shedding of liquid water from melting ice and from excessive amounts of water accumulated on supercooled frozen drops/hail; (5) preventing unrealistically large glaciation rates immediately above the freezing level by explicitly calculating freezing rates of raindrops and freezing rates of liquid water accreted onto supercooled ice; (6) introducing fall speeds and size distributions for small ice crystals; (7) calculating radar reflectivities of particles with variable size distributions and liquid water coatings from Rayleigh theory; (8) basing conversion of particle number concentrations between hydrometeor species on preserving spectral characteristics of particle distributions rather than conserving their number concentrations (important). Details of these parameterized processes can be found in Ferrier (1993).

The three-class ice formulations perform well only in specific large-scale environments, such that tropical-maritime storms are better represented using the Lin *et al.* (1983) scheme as modified by Rutledge and Hobbs (1984) which substitutes slower falling graupel for hail (McCumber *et al.*, 1991; Tao *et al.*, 1991), whereas the unmodified Lin *et al.* scheme is preferred in simulating midlatitude-continental storms (Ferrier *et al.*, 1991; Tao *et al.*, 1993). Furthermore, reasonable agreement with the observations may be obtained only after trial and error adjustment of several tunable coefficients in these three-class ice schemes. Figure 9 shows the radar reflectivities of an intense mid latitude-continental COHMEX (COoperative Huntsville Meteorological Experiment) squall line and a mature tropical-maritime GATE squall line simulated using the 4ICE microphysics. The simulated reflectivities compare well against radar observations of the COHMEX storm (Adler *et al.*, 1990; Yeh *et al.*, 1990) and the GATE squall line (Zipser *et al.*, 1983; Szoke and Zipser, 1986; not shown here). The 4ICE parameterization is much improved over the three-class ice schemes in the ability to simulate the radar and microphysical structures of storms that develop in vastly different environments with minimal tuning.

4.2 Numerical Advection Schemes

A second- or fourth-order horizontal advection scheme was generally used in the model with a time step of 7.5 or 10 s. However, using second-order or higher-order accuracy advection schemes can introduce some difficulties because negative values arise in the solution (Soong and Ogura, 1973). This effect can be especially important in cases where the solution of the advection is used as input to nonlinear equations describing microphysical phenomena or inert tracers which can eventually lead to instability of the whole system (Smolarkiewicz, 1983). The use of upstream differencing or other low-order schemes (Soong and Ogura, 1973) would not produce dispersive "ripples" but would suffer from excessive numerical diffusion. Smolarkiewicz (1983) has reduced the implicit diffusion by using a second "upstream" step where a specifically defined velocity field leads to a new form of a positive definite advection scheme with small implicit diffusion. The positive definite advection scheme involves iterations and needs more computational resources. This scheme has been improved with multidimensional application (Smolarkiewicz, 1984) and a non-oscillatory option (Smolarkiewicz and Grabowski, 1990).

The 2-D version of the GCE model has tested this Multi-dimensional Positive Definite Advection Transport Algorithm (MPDATA) for a PRE-STORM squall line case. Three specific tests have been performed. The first one was that all scalar variables (θ , q_v , K_m and all five hydrometeor classes) used forward time differencing and the MPDATA for advection. The dynamic variables, u , v and w , used a second-order accurate advection scheme and a leapfrog time integration (kinetic energy semi-conserving method). In the GCE model code, the perturbed potential temperature was predicted and it could be negative. In application of MPDATA, a constant (large number) needs to be added on to θ' . This can cause some problems (*e.g.*, invariance and stability) as discussed in Smolarkiewicz and Clark (1986). Thus, the second test applied the MPDATA method to the water vapor and hydrometeors only. The third test used the leapfrog time integration and fourth-order space derivative scheme for scalar and dynamic variables. Table 6 shows total surface precipitation and its anvil portion from these three runs. Several observed features for the PRE-STORM squall system, such as the weakly evolving multicellular structure, the mesolow aloft, the squall pressure high, and the rear inflow from the midtroposphere, were simulated in all three runs. All three runs also indicate a gradual growth of anvil precipitation with time (Table 6). However, the runs with the positive definite advection scheme generated more stratiform rain as well as broadening

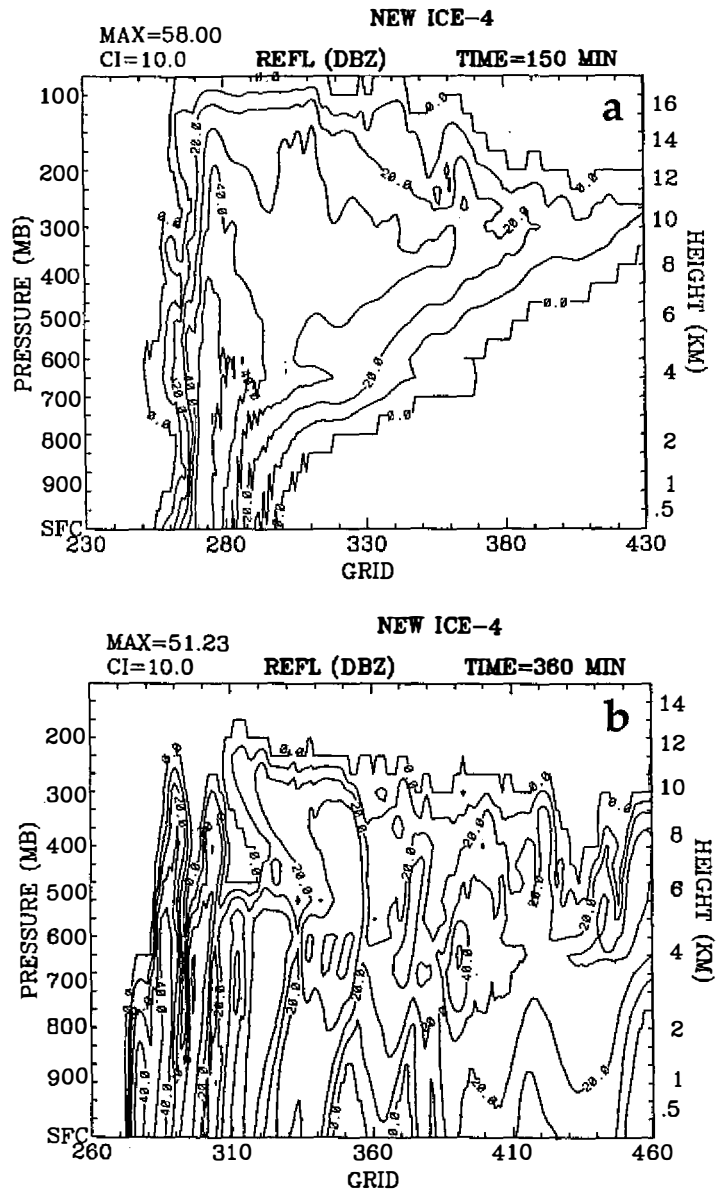


Fig. 9. Simulated radar reflectivities using the 4ICE scheme for (a) the 29 June 1986 COHMEX squall line at 150 min of the simulation time and (b) the 12 September 1974 (Day 255) GATE squall line 360 min into the simulation. A grid increment of $\Delta x=1$ km is used in both simulations. The COHMEX storm propagated eastward (to the right) and had a large leading (pre-line) anvil, whereas the GATE system propagated westward (to the left) and had an extensive area of trailing stratiform precipitation.

Table 6. Same as Table 3 except for the experiments with the positive definite advection (Smolarkiewicz) schemes and the fourth-order advection scheme.

(PRE-STORM Squall Line Simulations)

Time	MPDATA(1)		MPDATA(2)		4-th Order	
	Rain	Anvil	Rain	Anvil	Rain	Anvil
0-4h	2.76	8.6%	2.98	8.4%	2.55	7.7%
4-8h	5.43	24.5%	4.93	17.6%	4.80	16.3%
8-12h	5.90	27.5%	5.07	28.2%	4.60	20.8%
12-16h	4.85	33.4%	4.08	30.8%	2.82	31.0%
0-16h	18.94	25.4%	17.06	23.4%	14.77	19.0%

its horizontal extent (Figure 10). These features are in better agreement with observational studies (Johnson and Hamilton, 1988; and Rutledge *et al.*, 1988). The non-oscillatory option was used in the first runs, but oscillation in temperature still occurred in the first two runs. MPDATA as well as other positive-definite advection schemes will be tested for the new double-moment ice formulation in the near future.

4.3 Modeling the Interactions between Cloud Ensembles and Regional-scale Circulations

Observations of cumulus clouds generally indicate that clouds do not exist as isolated entities, but occur in groups or clusters. Observations also show that low-level mesoscale convergence (on the scale of 30-300 km) in a conditionally unstable environment is generally necessary to generate ensembles of deep convection (Ogura *et al.*, 1979; Simpson *et al.*, 1980). In general, numerical cloud model simulations have been initialized with an atmosphere having zero large-scale vertical velocity and with thermodynamic and horizontal wind profiles that are typical of the conditions upstream of severe convection (*e.g.*, Klemp and Wilhelmson, 1978; Schlesinger, 1978). Then, a perturbation is introduced by either a positive temperature anomaly at low levels (the "warm bubble" method) or by cooling the lowest layers (the "cold pool" method). Several different methods of inducing large-scale convergence have been described in the literature (Soong and Tao, 1980; Chen and Orville, 1980; Tripoli and Cotton, 1980; Tao, 1983; Dudhia and Moncrieff, 1987; Crook and Moncrieff, 1988, Tao and Simpson, 1989b; and others). One difficulty with these methods is that the large-scale convergence can only be evaluated before hand (a priori condition) from either observational or theoretical studies. It is important to note that in convective conditions, moist-convective processes can feed back (both positively and negatively) into the convergent forcing. For a model to approximate the real atmosphere, it should provide a convergence field that can vary in time and in space and also allow a feedback between the convection and the large-scale convergence field. In order to include this effect, either an eventual two-way nesting between a convective-scale and a mesoscale model or a much higher resolution capability (through an interactive grid nesting developed by Clark and Farley, 1984; and Chen, 1991) is needed.

The interaction between a mesoscale (GMASS, Goddard Mesoscale Atmospheric Simulation System) model and our convective scale (GCE) model is underway. We have modified

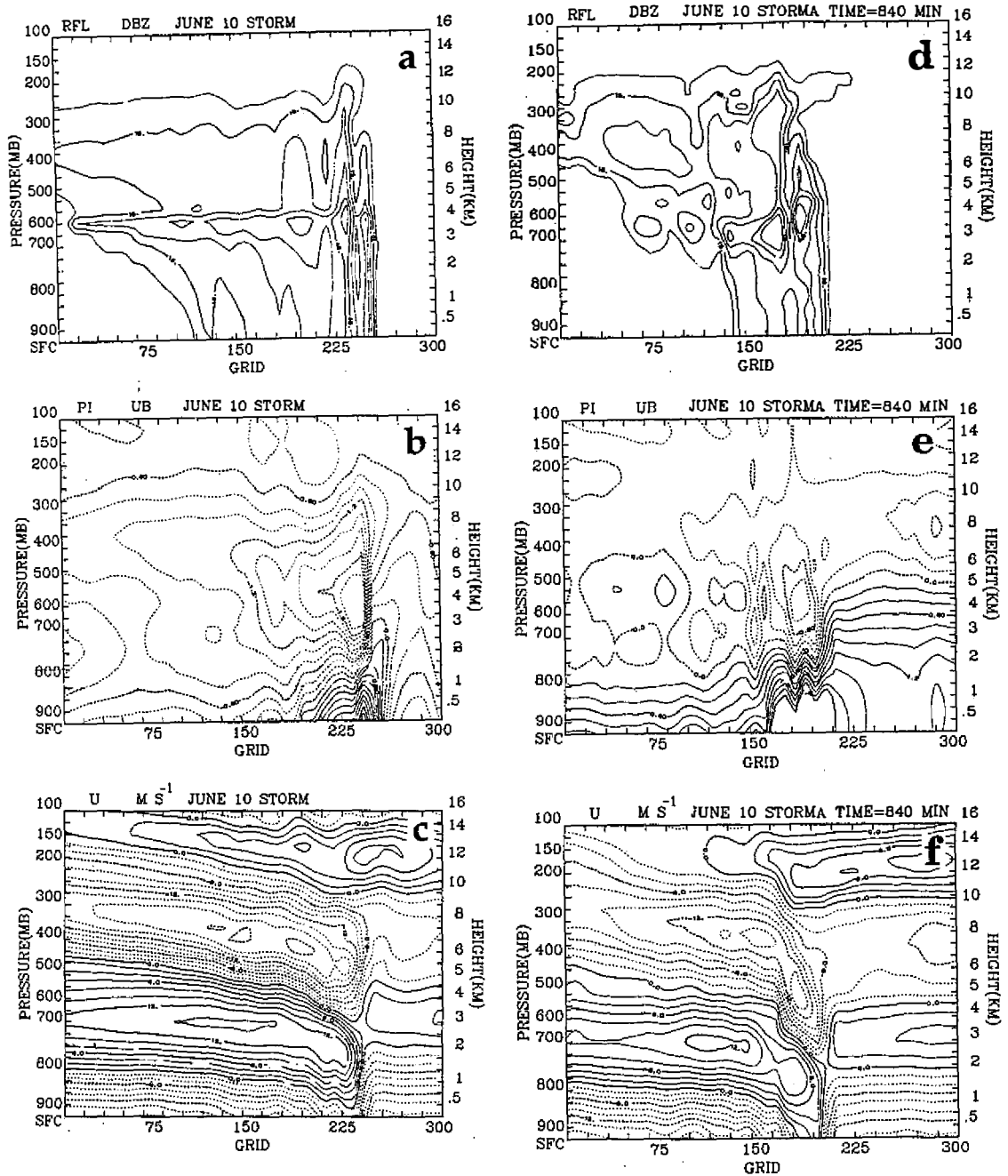


Fig. 10. Vertical cross section of (a) the simulated radar reflectivities, (b) the pressure deviation and (c) the wind speed relative to the squall line movement for the PRE-STORM run using the positive definite advection scheme (840 minutes into the simulation). The contour interval is 10 dBZ, 30 Pa and 2 m s^{-1} for (a), (b) and (c), respectively. Figs. 10 (d)-(f) are the same as Fig. 10 (a)-(c), respectively, except for a fourth-order advection scheme.

the GCE model to accept horizontally variable initial conditions provided by GMASS or analytic solutions (*e.g.*, solitary wave or Eady wave) using one-way open lateral boundary conditions. The buoyancy term in the w -equation (6) has been modified (the prime term is defined as a deviation from its initial value; not from its horizontal average). We also assume that only the perturbed wind (defined as a deviation from the initial value) will satisfy the continuity equation. Both the GCE model and GMASS have been initialized with the same analytic solutions to the Hoskins-Bretherton horizontal shear model at 60 h which is based on the semigeostrophic theory (*e.g.*, Hoskins and Bretherton, 1972). The horizontal domain size is equal to the wavelength of the most unstable baroclinic wave and periodic boundary conditions are used. The computed wave length and phase speed of the baroclinic wave are 3507 km (15 km resolution was used in the models) and 14.35 m s^{-1} , respectively. Both models have been tested under a dry environment (Biak *et al.*, 1992). Good qualitative agreement between GCE model and GMASS results have been found (Figure 11). The differences were mainly caused by an absorbing layer which was necessary for the non-hydrostatic model (in order to reduce the reflection of vertically propagating gravity waves). A much better agreement between the two models was obtained by applying the absorbing layer to θ' and w' only. We will examine similarities and differences in the simulated rainbands with full physics in both models. This comparison study will provide some indication as to how well the cumulus parameterizations perform in the mesoscale model. This kind of work is necessary to address the difficult problems that will be encountered in an eventual two-way nesting with GMASS.

The GCE model has also been initialized with a solitary wave (derived from nonlinear analytical theory by Dr. F. Einaudi at Goddard¹) as a test to see if convection could be triggered by such a mechanism as opposed to other methods. Preliminary results show that the model produced a realistic long-lasting cloud system compared with limited observations, such as echo top heights and propagation speeds derived from CHILL radar data and NMC

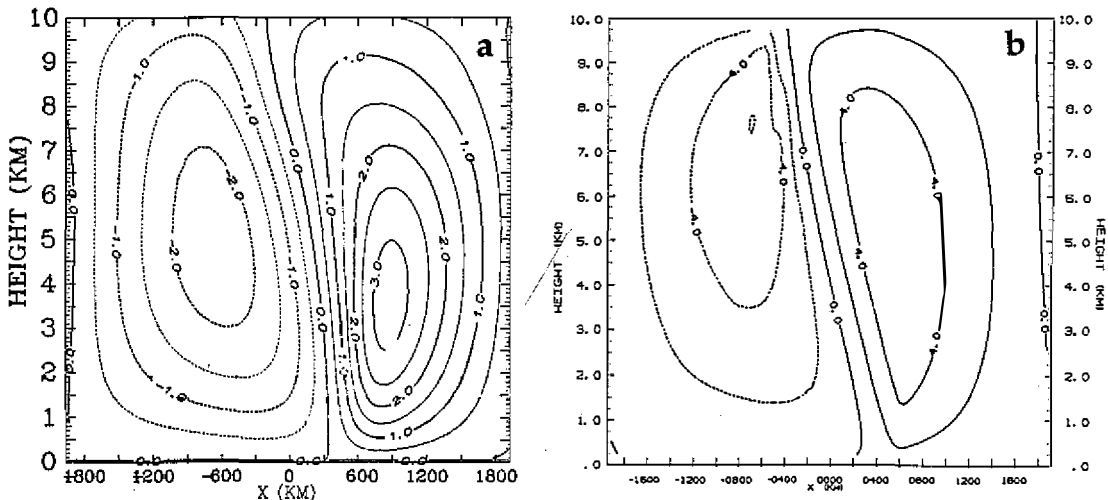


Fig. 11. Vertical cross section of w -velocity for the Eady simulation. (a) Non-hydrostatic (GCE) model, and (b) Hydrostatic (GMASS) model.

¹ Personal communication

radar summaries. It was found that an initial bubble is not necessary for cloud development but that the wave is indeed necessary to produce a long-lasting convective line. This result is consistent with those of Crook and Moncrieff (1988).

4.4 Land and Ocean Processes

An ocean mixed layer (OML) is couple with the GCE model to evaluate the effect of air-sea interaction on the development of atmospheric convective systems. The essential physics of the OML is similar to that of Kraus and Turner (1967) with some modifications (thermodynamic effects of salinity and precipitation). The GCE model-simulated diabatic source terms, radiation (Q_R), surface fluxes of sensible and latent heat, and the condensation minus evaporation in the atmosphere (net freshwater flux) were used as input for the OML model (see Sui *et al.*, 1991). Figure 12(a) is a schematic water budget of tropical cloud systems over the western Pacific Ocean. The total moisture supply (surface evaporation and large-scale advection), net latent heat release, radiative cooling/heating are normalized with respect to surface precipitation (or fresh water, P). The fresh water (P), net upward long wave radiation (I_o), turbulent flux of sensible heat flux (H_s) and net downward flux of solar radiation (R_o) are the drivers in the OML model. Figures 12(b) and (c) show that the ocean mixed layer structure maintained by the surface fluxes with and without fresh water falling into the ocean. A shallower mixed layer depth was found when fresh water was included. This result is in good agreement with measurements over the Western Pacific region (Sui *et al.*, 1993b).

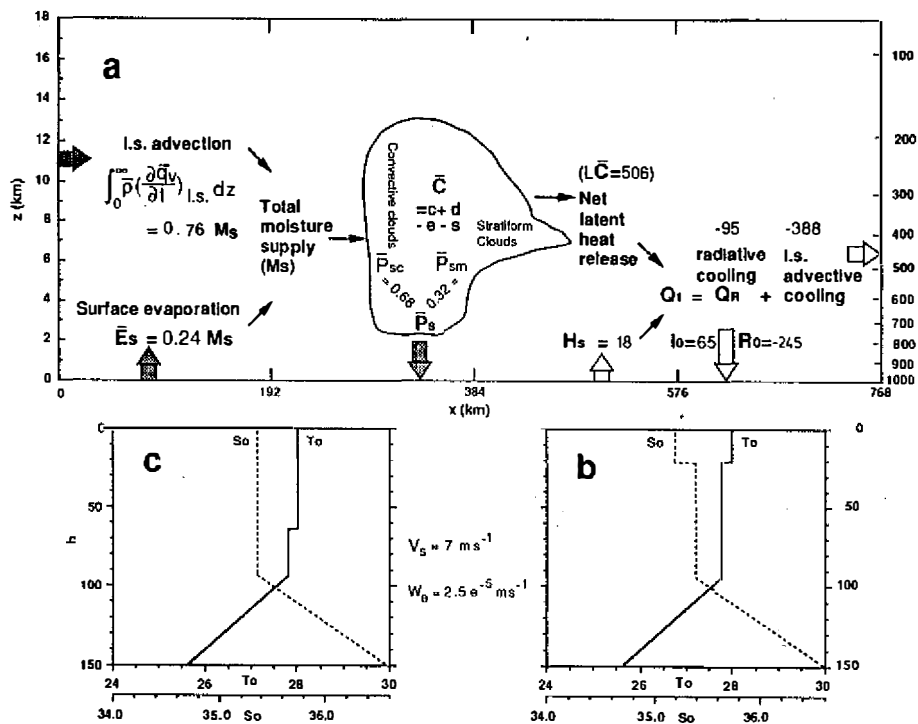


Fig. 12. (a) A summary of the ensemble mean heat and water budgets and the ocean mixed layer structure maintained by the surface fluxes with (b) and without (c) fresh water flux into the ocean.

Other key GCE model physics modifications are the addition of an energy balance equation for the ocean/land surface and incorporation of the high resolution Blackadar planetary boundary layer (PBL), which are currently used in GMASS. The effects of cloud-SST (Sea Surface Temperature)-radiation interaction will be estimated by performing a series of simulations with various SST's as well as land-ocean distributions. The inclusion of topography into the GCE model is also underway.

5. CONCLUSIONS AND FUTURE OUTLOOK

The GCE has evolved substantially over the past five years. Its applications to cloud ensembles in several different climatic regimes and to remote sensing of rainfall and associated latent heat release are discussed in Part II. It is clear that observations of cloud processes are greatly needed, particularly of ice-phase microphysics. A microphysical data set obtained in clouds over the Pacific warm ocean pool during TOGA/COARE will be especially valuable and will help to improve the formulations in the model.

It is recognized that bulk formulations of microphysics leave out important processes (such as particle sorting by differing fall speeds) which impact both the dynamical and radiative transfer aspects of convective systems. A close collaboration has been established with the groups of Kogan in Oklahoma U.S. and Rosenfeld in Israel who are working on explicit microphysics of both water and ice. The aim is to improve the bulk formulas by model-to-model comparison of results with detailed microphysics, since present computing capability does not permit many runs with a large number of size classes of hydrometeors. Since computing capability also limits simulation of scale interactions, improved boundary layer physics, and the allowable three-dimensional model domain, it is likely that a massive parallel processing approach will be required within the next few years.

Acknowledgments The authors thank Dr. S.-T. Soong, Dr. B. Ferrier, Dr. J. Scala, Mr. S. Lang, Dr. Sui, Dr. W. Lau, Dr. K. Pickering, Dr. A. Thompson, Dr. Moncrieff and Dr. C.-S. Chen for reading the manuscript and providing many useful suggestions.

The Goddard Cumulus Ensemble Model group is supported by the NASA Headquarters Radiation, Dynamics and Hydrology Branch under Contract 460-23-54 and by the NASA TRMM project under Contract 460-63-58. The authors are grateful to Drs. J. Theon and R. Kakar for their support of this research. Acknowledgment is also made to NASA/ Goddard Space Flight Center for computer time used in the research.

REFERENCES

- Adler, R., R. A. Mack, N. Prasad, H.-Y. Yeh and I. M. Hakkarinen, 1990: Aircraft microwave observations and simulations of deep convection from 18-183 GHz. Part I: Observations. *J. Atmos. Oceanic Technol.*, **7**, 377-391.
- Adler, R., N. Prasad, W.-K. Tao, H.-Y. Yeh, R. Mack and J. Simpson, 1988: Microwave observations and modeling of deep convection. In *Tropical Rainfall Measurements*, A. Deepak Publishing, 185-191.
- Adler, R. F., H.-Y. Yeh, N. Prasad, W.-K. Tao and J. Simpson, 1991: Microwave rainfall simulations of a tropical convective system with a three-dimensional cloud model. *J. Appl. Meteor.*, **30**, 924-953.

- Adler, R. F., J. Negri, N. Prasad, W.-K. Tao, 1989: Cloud model-based simulations of satellite microwave data and their application to an SSM/I algorithm. *Fourth Conf. on Satellite Meteorology and Oceanography*. San Diego, AMS, J12-J15.
- Anderson, J. R., K. K. Droegemeier and R. B. Wilhelmson, 1985: Simulation of the thunderstorm subcloud environment. Preprint, 14th *Conf. on Severe Local Storms*. 147-150.
- Biak, J.-J., M. C. McCumber, V. M. Karyampudi and S. E. Koch, 1992: Cold-frontal rain-band simulations using hydrostatic and non-hydrostatic models with explicit ice-phase microphysics. Preprints, 11th International Conf. on Clouds and Precipitation. Montreal, Canada, (in press).
- Chen, C., 1991: A nested-grid, non-hydrostatic, elastic model using a terrain-following coordinate transformation: The radiative-nesting boundary conditions. *Mon. Wea. Rev.*, **119**, 2852-2869.
- Chen, C.-H. and H. D. Orville, 1980: Effects of mesoscale convergence on cloud convection. *J. Appl. Meteor.*, **19**, 256-274.
- Chen, C.-S., 1980: The effect of the gust front on the generation of new convection. Ph.D., thesis, University of Illinois. 192 pp.
- Chen, C.-S., 1991: A numerical study of a squall line over the Taiwan Strait during TAMEX IOP 2. *Mon. Wea. Rev.*, **119**, 2677-2698.
- Chou, M.-D., 1984: Broadband water vapor transmission functions for atmospheric IR flux computation. *J. Atmos. Sci.*, **41**, 1775-1778.
- Chou, M.-D., 1986: Atmospheric solar heating rate in the water vapor bands. *J. Climate Appl. Meteor.*, **25**, 1532-1542.
- Chou, M.-D., 1992: A solar radiation model for use in climate studies. *J. Atmos. Sci.*, **49**, 762-772.
- Chou, M.-D. and A. Arking, 1980: Computation of infrared cooling rates in the water-vapor bands. *J. Atmos. Sci.*, **37**, 856-867.
- Chou, M.-D., and L. Kouvaris, 1991: Calculations of transmission functions in the IR CO₂ and O₃ Bands. *J. Geophys. Res.*, **96**, no. D5, 9003-9012.
- Clark, T. L., 1979: Numerical simulations with a three-dimensional cloud model: lateral boundary condition experiments and multicellular severe storm simulations. *J. Atmos. Sci.*, **36**, 2191-2215.
- Clark, T. L., and R. D. Farley, 1984: Severe downslope windstorm calculations in two and three spatial dimensions using anelastic interactive grid nesting: A possible mechanism gustiness. *J. Atmos. Sci.*, **41**, 329-350.
- Cotton, W. R. and G. J. Tripoli, 1978: Cumulus convection in shear flow-three-dimensional numerical experiments. *J. Atmos. Sci.*, **35**, 1053-1521.
- Crook, N. A. and M. Moncrieff, 1988: The effect of large-scale convergence on the generation and maintenance of deep moist convection. *J. Atmos. Sci.*, **45**, 3606-3624.
- Deardorff, J. W., 1973: Three-dimensional numerical modeling of planetary layer. *Workshop on Micrometeorology*, D. A. Haugen, Ed., Amer. Meteor. Soc., 217-311.
- Deardorff, J. W., 1975: The development of boundary-layer turbulence models for use in studying the severe storm environment. *Proceedings of the SESAME Opening Meeting*, Boulder, NOAA-ERL, 251-264.

- Dudhia, J., and M. W. Moncrieff, 1987: Numerical simulation of quasi-stationary tropical convective bands. *Quart. J. Roy. Meteor. Soc.*, **113**, 929-967.
- Ferrier, B. S., 1993: A double-moment multiple-phase four-class bulk ice parameterization. Part I: Description. *J. Atmos. Sci.*, (submitted).
- Ferrier, B. S., W-K. Tao, and J. Simpson, 1993: A double-moment multiple-phase four-class bulk ice parameterization. Part II: Simulations of convective systems in different large-scale environments and comparisons with other bulk parameterizations. *J. Atmos. Sci.*, (submitted).
- Ferrier, B. S., W.-K. Tao and J. Simpson, 1991: Radar and microphysical characteristics of convective storms simulated from a numerical model using a new microphysical parameterization. *25th International Conference on Radar Meteorology*, Paris, France, 782-785.
- Fovell, R. G., and Y. Ogura, 1988: Numerical simulation of a mid latitude squall line in two-dimensions. *J. Atmos. Sci.*, **45**, 3846-3879.
- Hoskins, B., J. and F. P. Bretherton, 1972: Atmospheric frontogenesis models: Mathematical formulation and solution. *J. Atmos. Sci.*, **29**, 11-37.
- Ikawa, M., 1988: Comparison of some schemes for non hydrostatic models with orography. *J. Meteor. Soc. Japan*, **66**, 753-776.
- Johnson, R. H. and P. J. Hamilton, 1988: The relationship of surface pressure features to the precipitation and airflow structure of an intense mid-latitude squall line. *Mon. Wea. Rev.*, **116**, 1444-1471.
- Klemp, J. B. and Wilhelmson, 1978: The simulation of three-dimensional convective storm dynamics. *J. Atmos. Sci.*, **35**, 1070-1096.
- Kraus, E. B. and J. S. Turner, 1967: A one-dimensional model of the seasonal thermocline: II. The general theory and its consequences. *Tellus*, **19**, 98-106.
- Lacis, A. A., and J. E. Hansen, 1974: A parameterization for absorption of solar radiation in the earth's atmosphere. *J. Atmos. Sci.*, **31**, 118-133.
- Lau, K. M., C. H. Sui and W.-K. Tao, 1993: Studies of the tropical hydrologic cycle using the cumulus ensemble model. *Bull. Amer. Meteor. Soc.*, (accepted).
- LeMone, M. A. and E. J. Zipser, 1980: Cumulonimbus vertical velocity events in GATE. Part I: Diameter, intensity and mass flux. *J. Atmos. Sci.*, **37**, 2444-2457.
- Lin, Y.-L., R. D. Farley and H. D. Orville, 1983: Bulk parameterization of the snow field in a cloud model. *J. Clim. Appl. Meteor.*, **22**, 1065-1092.
- McCumber, M., W.-K. Tao, J. Simpson, R. Penc, and S.-T. Soong, 1991: Comparison of ice-phase microphysical parameterization schemes using numerical simulations of tropical convection. *J. Appl. Meteor.*, **30**, 985-1004.
- Moncrieff, M. W., 1992: Organized convective systems: archetypal models, mass and momentum flux theory, and parameterization. *Quart. J. Roy. Meteor. Soc.*, **118**, (in press).
- Nicholls, M. E., 1987: A comparison of the results of a two-dimensional numerical simulation of a tropical squall line with observations. *Mon. Wea. Rev.*, **115**, 3055-3077.
- Ogura, Y. and N. A. Phillips, 1962: Scale analysis of deep and shallow convection in the atmosphere. *J. Atmos. Sci.*, **19**, 173-179.

- Ogura, Y., Y.-L. Chen, J. Russel and S.-T. Soong, 1979: On the formation of organized convective systems observed over the eastern Atlantic. *Mon. Wea. Rev.*, **107**, 426-441.
- Pickering, K. E., A. M. Thompson, J. R. Scala, W.-K. Tao, J. Simpson, and M. Garstang, 1991: Photochemical ozone production in Tropical squall line convection during NASA/GTE/ABLE 2A. *J. Geophys. Res.*, **96**, 3099-3114.
- Pickering, K. E., A. M. Thompson, J. R. Scala, W.-K. Tao, and J. Simpson, 1992a: Ozone production potential following convective redistribution of biomass emissions. *J. Atmos. Chem.*, **14**, 297-313.
- Pickering, K. E., J. Scala, A. M. Thompson, W.-K. Tao and J. Simpson, 1992b: A regional estimate of convective transport of CO from biomass burning, *Geophys Res. Letters*, Vol. **19**, No. 3, 289-292.
- Pickering, K. E., A. M. Thompson, J. Scala, W.-K. Tao, R. R. Dickerson and J. Simpson, 1992c: Free tropospheric ozone production following entrainment of urban plumes into deep convection, *J. Geophys Res.*, (in press).
- Ramaswamy, V. and V. Ramanathan, 1989: Solar absorption by cirrus clouds and the maintenance of the tropical upper troposphere thermal structure. *J. Atmos. Sci.*, **46**, 2293-2310.
- Riehl, H. and J. S. Malkus, 1958: On the heat balance in the equatorial trough zone. *Geophysica*, **6**, 503-535.
- Riehl, H. and J. Simpson, 1979: The heat balance of the equatorial trough zone, revisited. *Beitr. Phys. Atmos.*, **52**, 287-305.
- Roll, H. U., 1965: *Physics of the Marine Atmosphere*. Academic Press, 426 pp.
- Rotunno, R., J. B. Klemp and M. L. Weisman, 1988: A theory for strong, long-lived squall lines. *J. Atmos. Sci.*, **45**, 463-485.
- Rutledge, S. A., and P. V. Hobbs, 1984: The mesoscale and microscale structure and organization of clouds and precipitation in mid latitude clouds. Part XII: A diagnostic modeling study of precipitation development in narrow cold frontal rainbands. *J. Atmos. Sci.*, **41**, 2949-2972.
- Rutledge, S. A., R. A. Houze, Jr., M. I. Biggerstaff and T. Matejka, 1988: The Oklahoma-Kansas mesoscale convective system of 10-11 June 1985: Precipitation structure and single-Doppler radar analysis. *Mon. Wea. Rev.*, **116**, 1409-1430.
- Scala, J., M. Garstang, W.-K. Tao, K. Pickering, A. Thompson, J. Simpson, V. Kirchhoff, E. Browell, G. Sachse, A. Torres, G. Gregory, R. Rasmussen and M. Khalil, 1990: Cloud draft structure and trace gas transport. *J. Geophys. Res.*, **95**, 17015-17030.
- Schlesinger, R. E., 1978: A three-dimensional numerical model of an isolated thunderstorm. Part I: Comparative experiments of variable ambient wind shear. *J. Atmos. Sci.*, **35**, 690-713.
- Simpson, J., 1988: Tropical rainfall measuring mission (TRMM): A satellite mission to measure tropical rainfall. Report of the Science Steering Group, J. Simpson, Ed. NASA Publ., Govt. Printing Office, Washington, DC, 94 pp.
- Simpson, J. and W.-K. Tao, 1993: The Goddard Cumulus Ensemble Model. Part II: Applications for studying cloud precipitating processes and for NASA TRMM. *Terrestrial, Atmospheric and Oceanic Sciences*, **4**, 73-116.

- Simpson, J., R. F. Adler, and G. R. North, 1988: A proposed satellite tropical rainfall measuring mission (TRMM). *Bull. Amer. Meteor. Soc.*, **69**, 278-295.
- Simpson, J., N. E. Westcott, R. J. Clerman and R. A. Pielke, 1980: On cumulus mergers. *Arch. Meteor. Geophys. Bioklim.*, **A29**, 1-40.
- Smith, E. A. and A. Mugnai, 1989: Radiative transfer in space through a precipitating cloud at multiple microwave frequencies. Part III: Influence of large ice particles. *J. Meteor. Soc. Japan*, **67**, 739-755.
- Smolarkiewicz, P. K., 1983: A simple positive definite advection scheme with small implicit diffusion. *Mon. Wea. Rev.*, **111**, 479-486.
- Smolarkiewicz, P. K., 1984: A fully multidimensional positive definite advection transport algorithm with small implicit diffusion. *J. Comput. Phys.*, **54**, 325-362.
- Smolarkiewicz, P. K., and T. L. Clark, 1986: The multidimensional positive advection transport algorithm: Further development and applications. *J. Comput. Phys.*, **67**, 396-438.
- Smolarkiewicz, P. K., and W. W. Grabowski, 1990: The multidimensional positive advection transport algorithm: Nonoscillatory option. *J. Comput. Phys.*, **86**, 355-375.
- Soong, S.-T., and Y. Ogura, 1973: A comparison between axisymmetric and slab symmetric cumulus models. *J. Atmos. Sci.*, **30**, 879-893.
- Soong, S.-T., and Y. Ogura, 1980: Response of trade wind cumuli to large-scale processes. *J. Atmos. Sci.*, **37**, 2035-2050.
- Soong, S.-T., and W.-K. Tao, 1980: Response of deep tropical clouds to mesoscale processes. *J. Atmos. Sci.*, **37**, 2016-2036.
- Soong, S.-T., and W.-K. Tao, 1984: A numerical study of the vertical transport of momentum in a tropical rainband. *J. Atmos. Sci.*, **41**, 1049-1061.
- Stamnes, K., S.-C. Tsay, W. Wiscombe, and K. Jayaweera, 1988: Numerically stable algorithm for discrete-ordinate-method radiative transfer in multiple scattering and emitting layer media. *Appl. Optics*, **27**, 2502-2509.
- Star, D. O'C and S. K. Cox, 1985: Cirrus clouds. Part I: A cirrus cloud model. *J. Atmos. Sci.*, **42**, 2663-2681.
- Stephens, G. L., 1978, Radiative profiles in extended water clouds. Part II: Parameterization schemes. *J. Atmos. Sci.*, **35**, 2123-2132.
- Stephens, G. L., 1984: The parameterization of radiation for numerical weather prediction and climate models. *Mon. Wea. Rev.*, **112**, 826-867.
- Sui, C.-H., K.-M. Lau, W.-K. Tao, J. Simpson and M.-D. Chou, 1993a: Simulated heat, water and radiation budgets in the tropics. Part I: Model responses in a convective regime. *J. Atmos. Sci.*, (submitted).
- Sui, C.-H., K.-M. Lau, W.-K. Tao and J. Simpson, 1993b: Simulated heat, water and radiation budgets in the tropics. Part II: Climate implication. *J. Atmos. Sci.*, (to be submitted).
- Sui, C.-H., K.-M. Lau and A. K. Betts, 1991: An equilibrium model for the coupled ocean-atmospheric boundary layer in the tropics. *J. Geophys. Res.*, **96**, 3151-3163.
- Szoke, E. J. and E. J. Zipser, 1986: A radar study of convective cells in mesoscale systems in GATE. Part II: Life cycles of convective cells. *J. Atmos. Sci.*, **43**, 198-218.

- Tao, W.-K., 1983: A numerical study of the structure and vertical transport properties of a tropical convective system. Ph.D. Dissertation, Department of Atmospheric Science, University of Illinois, 228 pp.
- Tao, W.-K., and J. Simpson, 1984: Cloud interactions and merging: Numerical simulations. *J. Atmos. Sci.*, **41**, 2901-2917.
- Tao, W.-K., and J. Simpson, 1989a: A further study of cumulus interaction and mergers: Three-dimensional simulations with trajectory analyses. *J. Atmos. Sci.*, **46**, 2974-3004.
- Tao, W.-K., and J. Simpson, 1989b: Modeling study of a tropical squall-type convective line. *J. Atmos. Sci.*, **46**, 177-202.
- Tao, W.-K., and S.-T. Soong, 1986: A study of the response of deep tropical clouds to mesoscale processes: Three-dimensional numerical experiments. *J. Atmos. Sci.*, **43**, 2653-2676.
- Tao, W.-K., J. Simpson and M. McCumber, 1989: An ice-water saturation adjustment. *Mon. Wea. Rev.*, **117**, 231-235.
- Tao, W.-K., J. Simpson and S.-T. Soong, 1991: Numerical simulation of a subtropical squall line over Taiwan Strait. *Mon. Wea. Rev.*, **119**, 2699-2723.
- Tao, W.-K., J. Simpson, C.-H. Sui, S. Lang, J. Scala, B. Ferrier, M.-D. Chou and K. Pickering, 1993: Heating, moisture and water budgets of tropical and mid latitude squall lines: Comparisons and sensitivity to long wave radiation. *J. Atmos. Sci.* **50**, 673-690.
- Tao, W.-K., J. Simpson, and S.-T. Soong, 1987: Statistical properties of a cloud ensemble: A numerical study. *J. Atmos. Sci.*, **44**, 3175-3187.
- Tripoli, G. J., and W. R. Cotton, 1980: A numerical investigation of several factors contributing to the observed variable intensity of deep convection over south Florida. *J. Appl. Meteor.*, **19**, 1037-1063.
- Yeh, H.-Y. M., N. Prasad, W.-K. Tao, J. A. Jones, R. Meneghini, and R. F. Adler, 1992: Infrared, microwave, and spaceborne radar simulations of a deep convective system using a 3-D cloud ensemble model. *Sixth Conference on Satellite Meteorology and Oceanography*, Jan. 5-10, 1992, Atlanta, Ga, 226-229.
- Yeh, H.-Y. M., N. Prasad, R. A. Mack and R. F. Adler, 1990: Aircraft microwave observations and simulations of deep convection from 18-183 GHz. Part II: Model results. *J. Atmos. Oceanic Technol.*, **7**, 392-410.
- Yoshizaki, M., 1986: Numerical simulations of tropical squall-line clusters: Two-dimensional model. *J. Meteor. Soc. Japan*, **64**, 469-491.
- Zipser, E. J. and M. A. LeMone, 1980: Cumulonimbus vertical velocity events in GATE. Part II: Synthesis and model core structure. *J. Atmos. Sci.*, **37**, 2458-2469.
- Zipser, E. J., Y.-L. Chen and E. J. Szoke, 1983: On the generation of heavy precipitation within the anvil system of a tropical squall line. *Proceedings, 21th Conf. on Radar Meteorology, Edmonton, AMS.*, 50-56.

Appendix

Acronyms

ABLE Amazon Boundary Layer Experiment
AMEX Australian Monsoon Experiment
CAPE Convective and Precipitation/Electrification Experiment
CHILL CHicago ILLinois
COHMEX Cooperative Huntsville Meteorological Experiment
COPT-81 Convection Profonde Tropicale, 1981
EMEX Equatorial Mesoscale Experiment
ENSO El Nio/Southern Oscillation
EOS Earth Observing System
FFT Fast Fourier Transform
FGGE First GARP (Global Atmospheric Research Program)

Global Experiment

FSU Florida State University
GATE GARP (Global Atmospheric Research Program) Atlantic Tropical Experiment
GCE model Goddard Cumulus Ensemble model
GCM General Circulation Model
GEWEX Global Energy and Water Cycle Experiment
GMASS Goddard Mesoscale Atmospheric Simulation System
GLA Goddard Laboratory for Atmospheres
GTE Global Tropospheric Experiment
ITCZ Inter Tropical Convergence Zone

Acronyms cont.

MCS Mesoscale Convective System
MPDATA Multi-dimensional Positive Definite Advection Transport Algorithm
NASA National Aeronautics and Space Administration
NCAR National Center for Atmospheric Research
NMC National Meteorological Center
OML Ocean Mixed Layer
PBL Planetary Boundary Layer
PRESTORM Preliminary Regional Experiment for STORM - Central
SCC Super-Cloud-Cluster
SSM/I Special Sensor Microwave/Imager
SST Sea Surface Temperature
STEP Stratospheric Troposphere Exchange Program
STORM STormscale Operational and Research Meteorology
TAMEX Taiwan Area Mesoscale Experiment
TOGA-COARE Tropical Ocean-Global Atmosphere Program-Coupled Ocean-
Atmosphere Response Experiment
TRMM Tropical Rainfall Measuring Mission
WMONEX Winter Monsoon Experiment 1Personal communication

